

# Direct computation of aeroacoustic fields in laminar flows: solver development and assessment of wall temperature effects on radiated sound around bluff bodies

Valerio D'Alessandro<sup>a,\*</sup>, Matteo Falone<sup>a</sup>, Renato Ricci<sup>a</sup>

<sup>a</sup>*Dipartimento di Ingegneria Industriale e Scienze Matematiche  
Università Politecnica delle Marche  
Via Brecce Bianche, 60131 Ancona (AN), Italy*

---

## Abstract

This work presents results of a direct computation of acoustic fields produced by several laminar flow configurations. A solver specifically developed for compressible mass, momentum and energy equations, named `caafoam`, is presented. Low-storage high-order Runge-Kutta schemes were used for time integration, and an unstructured colocated finite-volume method for space discretization. A sponge-layer-type non-reflective boundary treatment was adopted to avoid spurious numerical reflections at the far-field boundaries. These techniques were chosen and tested to see if they enable a broad range of physical phenomena, with a particular emphasis on aeroacoustic problems, to be solved. The reliability, efficiency and robustness of `caafoam` was demonstrated by computing several benchmarks concerning far-field aerodynamic sound. After proving the direct simulation capabilities of `caafoam`, it was used to analyze the effect of the wall temperature conditions on the aeroacoustic sound produced by laminar flows over bluff bodies.

*Key words:*

OpenFOAM, Aeroacoustics, Direct Numerical Simulation, Bluff body, Active sound reduction

---

## 1 Introduction

The study of noise radiated from objects is a key engineering problem because the noise itself can have significant negative effects on our daily lives.

---

\* Corresponding author.

*Email address:* v.dalessandro@univpm.it (Valerio D'Alessandro).

From the engineering standpoint, it is essential to understand the mechanisms of aeroacoustic noise generation and propagation in order to achieve its control/reduction. A number of experimental efforts have been devoted to this issue, but they have met with a few problems relating to aeroacoustic noise. It is really difficult, for instance, to remove background noise that contaminates the aeroacoustic field.

Computational aeroacoustic (CAA) techniques can be a reliable way to study aerodynamically-produced sound [1]. They involve several approaches; however our interests are devoted to the direct numerical simulation (DNS) of the aeroacoustic sound, where the flow generating the sound and its propagation are both solved computationally.

DNS can encounter several difficulties, largely because the sound pressure is usually much smaller than the ambient pressure [2]. In addition, acoustic waves are reflected at the far boundaries of the domain when standard boundary conditions are employed and, for DNS computations, ad hoc non-reflecting boundary conditions are needed to fix this issue [3]. To prevent numerical dissipation and dispersion from overshadowing sound production, DNS computations have traditionally been done using high-order methods, such as finite difference (FD) [4], finite volume (FV) [5] or, more recently, discontinuous Galerkin (DG) methods [6]. For the same reasons, Runge-Kutta (RK) methods are used for time integration. It is worth noting that high-order FD (based on compact schemes) and FV methods carry a loss of parallel efficiency due to a non-compact stencil. On the other hand, the theoretical order of accuracy is not preserved when dealing with irregular grids, or at the physical boundaries. DG methods are more flexible than FV or FD approaches, but they carry a huge computational resource demand [7]. High-order methods have been also employed by CAA investigators since they allow to resolve waves propagation phenomena with the minimum number of mesh points per wavelength [3]. Differently, standard second-order schemes require a grater number of mesh points per wavelength to ensure adequate accuracy. Thus, they are not considered as the cutting-edge solution strategy in CAA.

All the above-mentioned high-resolution methods are typically adopted in academic codes with a very limited dissemination to the general public. That is why we have developed an open-source solver for aeroacoustic DNS to publicize the feasibility of performing such computations. Our CAA solver, named `caafoam`, is free to download on GitHub at the following address: <https://github.com/vdalessa/caafoam>. It employs low-storage high-order Runge-Kutta (RK) schemes for time integration, with an accurate artificial sponge-layer-type, non-reflective boundary treatment. The governing equations are space-discretized using an unstructured colocated FV method in order to exploit the solver's flexibility in handling complex geometries. Moreover, our second order approach is also intended as extending the OpenFOAM library capabilities for CAA and compressible flows and it is also conceived as a stepping stone to higher order implementations in OpenFOAM.

The solver has been validated, also by comparing its performance with other

freely-available tools, to demonstrate its reliability, efficiency and robustness. Particularly, in the considered cases the sound radiated from bluff bodies in a uniform undisturbed flow is directly simulated.

The impact of the thermal boundary conditions on sound propagation is also investigated. It was shown that the wall temperature increment can reduce the lift and drag pulsations and increase the drag generated by the Karman vortex street that is shed over bluff bodies in laminar flows. In the available literature, similar effects had already been noted by Lecordier et al. [8, 9]. In the present context, however, any reduction in lift pulsations is very important because it leads to a decay in aeroacoustic perturbations.

This paper is organised as follows: the governing equations are presented in Section 2, while the adopted numerical discretization techniques are discussed in Section 3; Section 4 is devoted to numerical results. Lastly, Section 5 contains the conclusions.

## 2 Governing equations

The flow model adopted in this work concerns the unsteady mass,momentum and energy equations. Let  $t \in [0, T]$  be a given instant in the temporal domain,  $\mathbf{x} \in \Omega \subset \mathbb{R}^d$  (with  $d = 2, 3$ ) a given point in the spatial domain, and  $Q = \Omega \times [0, T] \subset \mathbb{R}^d \times \mathbb{R}^+$ . The initial boundary values problem consists in finding the solution vector  $\mathbf{u} : Q \rightarrow \mathbb{R}^{d+2}$  that, for the given Dirichelet boundary conditions  $\mathbf{u}_D : \Gamma_D \times [0, T] \rightarrow \mathbb{R}^{d+2}$ , Neumann boundary conditions  $\mathbf{h}_N : \Gamma_N \times [0, T] \rightarrow \mathbb{R}^{d+2}$ , and initial conditions  $\mathbf{u}_0 : \Omega \rightarrow \mathbb{R}^{d+2}$ , satisfy the governing equations:

$$\begin{aligned} \frac{\partial \mathbf{u}}{\partial t} + \frac{\partial \mathbf{f}_{\mathbf{c},j}}{\partial x_j} &= \frac{\partial \mathbf{f}_{\mathbf{v},j}}{\partial x_j} && \text{in } Q, \\ \mathbf{u} &= \mathbf{u}_D && \text{on } \Gamma_D \times [0, T], \\ \frac{\partial \mathbf{u}}{\partial x_j} n_j &= \mathbf{h}_N && \text{on } \Gamma_N \times [0, T], \\ \mathbf{u} &= \mathbf{u}_0 && \text{in } \Omega \subset \mathbb{R}^d, t = 0, \end{aligned} \tag{1}$$

where  $\Gamma = \Gamma_D \cup \Gamma_N$  is the boundary of the domain  $\Omega$ ;  $\Gamma_D$  and  $\Gamma_N$  are the Dirichelet and Neumann boundaries, respectively; and  $n_j$  are the components of the outward-facing unit normal vector on  $\Gamma$ .

Relying on the vector  $\mathbf{u} = (\rho, \rho u_1, \rho u_2, \rho u_3, \rho E)^T$ , the j-th component of the

convective and diffusive fluxes reads:

$$\mathbf{f}_{\mathbf{c},j} = \begin{pmatrix} \rho u_j \\ \rho u_1 u_j + p \delta_{1j} \\ \rho u_2 u_j + p \delta_{2j} \\ \rho u_3 u_j + p \delta_{3j} \\ \rho u_j H \end{pmatrix}, \quad \mathbf{f}_{\mathbf{v},j} = \begin{pmatrix} 0 \\ \tau_{1j} \\ \tau_{2j} \\ \tau_{3j} \\ \tau_{ji} u_i - q_j \end{pmatrix}. \quad (2)$$

In these relations,  $\rho$  denotes the density,  $u_i$  is the generic Cartesian component of the velocity vector  $\mathbf{v}$ , and  $p$  is the pressure.  $E$  is the total internal energy, while the total enthalpy is obtained from  $H = E + p/\rho$ . The viscous stress tensor is computed using the standard constitutive relation for Newtonian fluids:

$$\tau_{ij} = \mu \left( \frac{\partial u_i}{\partial x_j} + \frac{\partial u_j}{\partial x_i} \right) - \frac{2}{3} \mu \frac{\partial u_k}{\partial x_k} \delta_{ij} \quad (3)$$

and the heat flux vector components by means of the Fourier postulate:  $q_i = -\lambda \frac{\partial T}{\partial x_i}$ . Note that  $\mu$  is the dynamic viscosity and  $\lambda$  the thermal conductivity which in this work are modeled as temperature independent. The fluid temperature,  $T$ , is measured starting from the total internal energy as follows:  $c_v T = E - \frac{1}{2} \mathbf{v} \cdot \mathbf{v}$ , where  $c_v$  is the specific heat at constant volume. Lastly, the pressure is computed by adopting the ideal gas equation of state as a thermodynamic model:  $p = \rho (\gamma - 1) (E - \frac{1}{2} \mathbf{v} \cdot \mathbf{v})$ , where  $\gamma = c_p/c_v$  is the specific heat ratio of the fluid.

## 2.1 Non-reflective boundary treatment

As discussed in Section 1, to compute acoustic wave propagation phenomena we need to avoid spurious numerical sound waves produced by external boundaries of the domain. An artificial sponge layer [10, 11] is used for this purpose. The sponge treatment has been widely used because it is simple, robust and flexible in handling complex geometries [12]. Taking this approach, the governing equations are modified as follows:

$$\frac{\partial \mathbf{u}}{\partial t} + \frac{\partial \mathbf{f}_{\mathbf{c},j}}{\partial x_j} - \frac{\partial \mathbf{f}_{\mathbf{v},j}}{\partial x_j} = \sigma (\mathbf{u}_{ref} - \mathbf{u}) \quad \text{in } Q \quad (4)$$

The new non-physical term on the right-hand side of eq. 4 is only active near the external boundaries, where it dampens the flow variables to a known reference solution,  $\mathbf{u}_{ref}$ . In eq. 4, the scalar field  $\sigma : \Omega \rightarrow \mathbb{R}$  is:

$$\sigma = \sigma_0 \left( \frac{L_{sp} - d}{L_{sp}} \right)^n \quad (5)$$

where  $L_{sp}$  is the thickness of the layer,  $d$  is the minimum distance from the nearest far-field boundary,  $\sigma_0$  is a constant value, and  $n$  is an integer parameter controlling the shape of the sponge's profile. An optimal sponge layer design is not trivial: larger sponges perform better than equally-strong smaller ones. In other words, they dampen flow features more quietly [13]. Larger sponges demand larger computational domains; indeed they must be positioned far enough away from the sound sources to avoid interference phenomena with the flow/acoustic fields.

Another possible non-reflective approach consists in the adoption of sponge-layers which exploit the numerical dissipation produced by the grid stretching. Despite its conceptual simplicity this technique poses difficulties with regard to the evaluation of the grid stretching entity and grid cells' number needed to be applied in the buffer zone. The specific choice is often related to the computational experience gained on a particular code [14]. For this reason in the following we prefer polynomial sponge-layers.

Mani [13] recently ran a theoretical and numerical analysis on non-reflecting boundary treatments based on polynomial sponge layers. The Author provided several practical guidelines for CFD/CAA practitioners on how to avoid sponge failure. In particular, the non-reflective boundary implementation is based on the following parameter:

$$\eta_{target} = -\frac{40 \log_{10} e}{1 - M_\infty^2} \int_{L_{sp}} \sigma d\mathbf{x}, \quad (6)$$

where  $\eta_{target}$  is the sponge's strength expressed in dB, and  $M_\infty$  is the Mach number of the undisturbed flow. As an example, a sponge with a strength of 40 dB would dampen the amplitude of an incident sound wave by a factor of 100 under one-dimensional conditions. The sponge's thickness must also be established with the following constraint:

$$0.5 \leq \frac{L_{sp} \cdot f}{c_\infty} \leq 2 \quad (7)$$

where  $f$  is the sound disturbance frequency, and  $c_\infty$  is its phase speed [13]. For all the computations presented in this paper, we have observed that  $\eta_{target} = 40$  dB is needed, so  $n = 2$  in eq. 5 has been selected. Indeed, Mani [13] investigated the effect of  $n$  on the sponge performance and it showed that quadratic sponge has best overall performance for  $\eta_{target}$  ranging from 20 dB to 60 dB. Lastly, the dimensionless parameter  $(L_{sp} \cdot f) / c_\infty$ , strictly needed to evaluate sponge width, is fixed equal to 0.5 to limit the computational load.

## 2.2 Computing the distance from far-field boundaries

For the purpose of establishing the distance from far-field (non-reflective) boundaries, we have solved the Eikonal differential equation:

$$\frac{\partial \varphi}{\partial x_j} \frac{\partial \varphi}{\partial x_j} = 1 \quad \text{in } \Omega, \quad (8)$$

where  $\varphi : \Omega \rightarrow \mathbb{R}$  is the distance field. A homogeneous Dirichelet condition is imposed on the non-reflective boundaries, and a homogeneous Neumann boundary condition elsewhere.

The Eikonal equation computes the exact distance, defined as the distance from the boundary normal direction. In other words, the distance can be seen as an advancing front with a unit velocity in the direction of the boundary normal. The main advantage of this technique is its good scalability on larger meshes.

The solution for eq. 8 has thus been obtained by converting it into a hyperbolic problem, adding a pseudo-time term:

$$\frac{\partial \varphi}{\partial \tau} + u_{\varphi,j} \frac{\partial \varphi}{\partial x_j} = 1 \quad \text{in } Q \quad (9)$$

with  $u_{\varphi,j} = \partial \varphi / \partial x_j$ . The solver for computing far-field distance, named `eikonal`, is free to download at <https://github.com/vdalessa/eikonal>. It only has to be run once in the pre-processing stage because we rely on non-moving meshes.

## 3 Numerical approximation

### 3.1 Finite volume discretization

In the unstructured, colocated, cell-centered FV method adopted in this work, the computational domain  $\Omega$  is divided into a set of non-overlapping polygonal cells. Finite volume discretization is briefly recalled here as it is crucial to discussing the approximation techniques for each term appearing in the discrete equations. In the following expressions, the values of the variables at the center of the cell faces are indicated with the subscript  $(\cdot)_f$ . The term  $\mathbf{S}_f$  is the surface area vector of each mesh face; see Fig. 1 for a schematic representation.

Starting from the integration of eq. 4 over each mesh element,  $K$  (having boundary  $\partial K$ ), we obtain:

$$\int_K \frac{\partial \mathbf{u}}{\partial t} d\Omega + \int_{\partial K} (\mathbf{f}_{\mathbf{c},j} - \mathbf{f}_{\mathbf{v},j}) n_j d\Gamma = \int_K \sigma (\mathbf{u}_{ref} - \mathbf{u}) d\Omega. \quad (10)$$

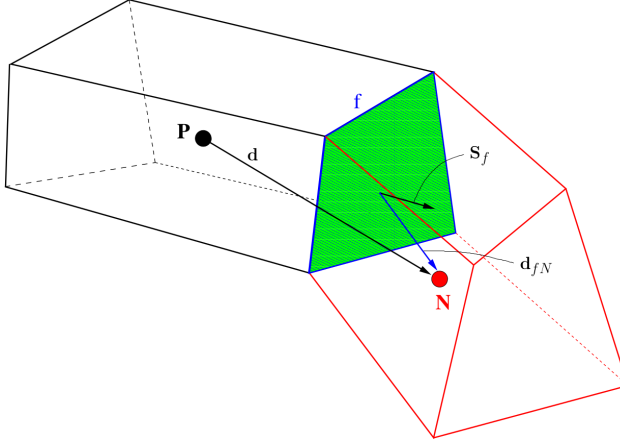


Figure 1. The computational cells.

The non-linear convective term is discretized as follows:

$$\int_{\partial K} \mathbf{f}_{c,j} n_j \, d\Gamma = \sum_{f=1}^{N_f} (\mathbf{f}_{c,j})_f n_j |\mathbf{S}_f| \quad (11)$$

where  $N_f$  is the number of faces belonging to the mesh element  $K$ . Rewriting the Eulerian terms vector as:

$$\mathbf{f}_{c,j} = u_j \mathbf{u} + \mathbf{f}_{c_p,j} + \mathbf{f}_{c_E,j} \quad (12)$$

with  $\mathbf{f}_{c_p,j} = (0, p\delta_{1j}, p\delta_{2j}, p\delta_{3j}, 0)^T$  and  $\mathbf{f}_{c_E,j} = (0, 0, 0, 0, u_j p)^T$ , it can be approximated as follows:

$$\sum_{f=1}^{N_f} (\mathbf{f}_{c,j})_f n_j |\mathbf{S}_f| = \sum_{f=1}^{N_f} \phi_f \mathbf{u}_f + \sum_{f=1}^{N_f} \Lambda_f^{(1)} |\mathbf{S}_f| + \sum_{f=1}^{N_f} \phi_f \Lambda_f^{(2)} \quad (13)$$

where  $\Lambda_f^{(1)} = (0, p, p, p, 0)^T$  and  $\Lambda_f^{(2)} = (0, 0, 0, 0, p)^T$ . A first way to handle the three terms on the right-hand side of eq. 13 that we consider here follows the Kurganov-Noelle-Petrova (KNP) approach [15]:

$$\begin{aligned} \sum_{f=1}^{N_f} \phi_f \mathbf{u}_f &= \sum_{f=1}^{N_f} \frac{(\psi \phi \mathbf{u})_f^+ - (\psi \phi \mathbf{u})_f^-}{\psi_f^+ + \psi_f^-} + \frac{\psi_f^+ \psi_f^-}{\psi_f^+ + \psi_f^-} (\mathbf{u}_f^+ + \mathbf{u}_f^-), \\ \sum_{f=1}^{N_f} \Lambda_f^{(1)} \mathbf{S}_f &= \sum_{f=1}^{N_f} \frac{\psi_f^+}{\psi_f^+ + \psi_f^-} |\mathbf{S}_f| (\Lambda^{(1)})_f^+ + \frac{\psi_f^-}{\psi_f^+ + \psi_f^-} |\mathbf{S}_f| (\Lambda^{(1)})_f^-, \\ \sum_{f=1}^{N_f} \Lambda_f^{(2)} \mathbf{S}_f &= \sum_{f=1}^{N_f} \frac{(\psi \phi \Lambda^{(2)})_f^+ - (\psi \phi \Lambda^{(2)})_f^-}{\psi_f^+ + \psi_f^-}. \end{aligned} \quad (14)$$

Note that the term  $\phi_f$  in the above equation represents the velocity flux through the cells' face, and it is evaluated as:  $\phi_f = \mathbf{v}_f \cdot \mathbf{S}_f$ . In eq. 14, the

superscript + denotes the face value of the element placed in the direction parallel to the  $\mathbf{S}_f$  vector depicted in Fig. 1; and the superscript – the opposite direction. These values are obtained by means of a linear interpolation; for example, the + interpolation for  $\mathbf{u}_f$ , *i.e.*  $\mathbf{u}_f^+$ , is simply:

$$\mathbf{u}_f^+ = \left(1 - \frac{\mathbf{S}_f \cdot \mathbf{d}_{fN}}{|\mathbf{S}_f| |\mathbf{d}_{fN}|}\right) \mathbf{u}_P + \frac{\mathbf{S}_f \cdot \mathbf{d}_{fN}}{|\mathbf{S}_f| |\mathbf{d}_{fN}|} \mathbf{u}_N, \quad (15)$$

the meaning of  $\mathbf{d}_{fN}$  is depicted in Fig. 1.  $\psi_f^+$  and  $\psi_f^-$  are associated with the local speed of propagation, and they are calculated as reported in Greenshields et al. [16]:

$$\begin{aligned} \psi_f^+ &= \max \left( |\mathbf{S}_f| \sqrt{\gamma R T_f^+} + \phi_f^+, |\mathbf{S}_f| \sqrt{\gamma R T_f^-} + \phi_f^-, 0 \right), \\ \psi_f^- &= \max \left( |\mathbf{S}_f| \sqrt{\gamma R T_f^+} - \phi_f^+, |\mathbf{S}_f| \sqrt{\gamma R T_f^-} - \phi_f^-, 0 \right), \end{aligned} \quad (16)$$

where  $R$  is the gas constant.

KNP scheme was selected since: (i) there are no Riemann solvers and characteristic decomposition involved [15]; (ii) it is already implemented within OpenFOAM package and repeatedly tested; so it produces a reliable approximate solution of the Riemann problem.

In this paper, we also consider a second approach to approximating the Eulerian numerical flux in which we split  $\mathbf{f}_{c,j}$  into a convective and a pressure part:

$$\mathbf{f}_{c,j} = \mathbf{f}_{c_{H,j}} + \mathbf{f}_{c_{p,j}} \quad (17)$$

with  $\mathbf{f}_{c_{H,j}} = u_j (\rho, \rho u_1, \rho u_2, \rho u_3, \rho H)^T$ ; so FV approximation for  $\mathbf{f}_{c,j}$  is:

$$\sum_{f=1}^{N_f} \left( \mathbf{f}_{c,j} \right)_f n_j |\mathbf{S}_f| = \sum_{f=1}^{N_f} \left( \mathbf{f}_{c_{H,j}} \right)_f n_j |\mathbf{S}_f| + \sum_{f=1}^{N_f} \left( \mathbf{f}_{c_{p,j}} \right)_f n_j |\mathbf{S}_f|. \quad (18)$$

The convective part of the Eulerian flux is computed here by following Pirozzi's energy-conserving scheme [17]:

$$\mathbf{f}_{c_{H,j}} = \frac{1}{8} (\rho^+ + \rho^-) (u_n^+ + u_n^-) (\boldsymbol{\varphi}^+ + \boldsymbol{\varphi}^-) \quad (19)$$

where  $\boldsymbol{\varphi} = (1, u_1, u_2, u_3, H)^T$  and  $u_n = u_j n_j$ . The pressure flux is obtained from:

$$\mathbf{f}_{c_{p,j}} = \frac{1}{2} \left( \mathbf{f}_{c_{p,j}}^+ + \mathbf{f}_{c_{p,j}}^- \right) + \mathbf{f}_{c_{p,j}}^D. \quad (20)$$

The diffusive part in the numerical flux of eq. 20,  $\mathbf{f}_{c_{p,j}}^D$ , is activated to increase the stability of the discretization technique in computations on unstructured or distorted meshes. In particular, to activate  $\mathbf{f}_{c_{p,j}}^D$  we rely on a classical shock

sensor, [18]:

$$\theta = \max \left( -\frac{\nabla \cdot \mathbf{v}}{\sqrt{(\nabla \cdot \mathbf{v})^2 + |\nabla \wedge \mathbf{v}|^2 + u_0^2/L_0^2}}, 0 \right) \quad \theta \in [0, 1] \quad (21)$$

where  $u_0$  and  $L_0$  are suitable velocity and length scales [19]. In the cases considered in this paper, as in Modesti and Pirozzoli [20], the artificial diffusion term is designed to be proportional to  $\theta_f = (\theta^+ + \theta^-)/2$ :

$$(\mathbf{f}_{\mathbf{c}_{\mathbf{p},j}}^D)_f = \alpha \theta_f (\mathbf{f}_{\mathbf{c}_{\mathbf{p},j}}^{\text{AUSM}})_f. \quad (22)$$

Note that  $\alpha$  is a flag controlling the activation of the diffusive pressure flux, while  $\mathbf{f}_{\mathbf{c}_{\mathbf{p},j}}^{\text{AUSM}}$  is obtained using the AUSM<sup>+</sup>-up formula (eqs. (69) to (77) of Liou [21]).

We also wish to mention that the Courant number, Co, is computed in this work using the following equation:

$$\text{Co} = \max(|\psi_f^+|, |\psi_f^-|) \frac{\delta \Delta t}{|\mathbf{S}_f|} \quad (23)$$

with:

$$\delta = \frac{1}{\max \left( \mathbf{d} \cdot \frac{\mathbf{s}_f}{|\mathbf{s}_f|}, 0.05 |\mathbf{d}| \right)}, \quad (24)$$

$\mathbf{d}$  as shown in Fig. 1.

Standard approximation schemes are used for the diffusive fluxes,  $\mathbf{f}_{\mathbf{v},j}$ . Since discussing such techniques is beyond the scope of this manuscript, we refer readers to the textbook by Ferzinger and Peric [22] for more details.

It is worth noting that flow problems with shock-waves are not considered in the presented numerical methodology. From here on, we refer to the KNP-based solver as **caafoam-m1**, while **caafoam-m2** is used to indicate the solver based on Pirozzoli's scheme.

Lastly, we want to point out that Eikonal equation is solved in its hyperbolic form, eq. 9, using a fully explicit approach. Standard central schemes have been employed for this purpose for structured grids, while upwind techniques have been used for unstructured meshes since in this case the former approach is unstable.

### 3.2 Time integration schemes

For each FV, the interpolation coefficients obtained from the discretization process are used to form the following system of ODEs:

$$\frac{d\mathbf{U}}{dt} = \mathbf{R}(\mathbf{U}) \quad (25)$$

where  $\mathbf{R}$  is the residual of the space discretization including the convective, diffusive and source terms; and  $\mathbf{U}$  is the degrees of freedom (DoFs) vector.

Explicit Runge-Kutta (ERK) schemes were used to solve eq. 25 in the present work. The ERK Williamson formula [23] was implemented to contain memory usage. The integration strategy in the  $k$ -th RK stage can be summarized as:

$$\begin{aligned}\Delta \mathbf{U}^{(k)} &= A_k \Delta \mathbf{U}^{(k-1)} + \Delta t \mathbf{R}(\mathbf{U}^{(k-1)}), \\ \mathbf{U}^{(k)} &= \mathbf{U}^{(k-1)} + B_k \Delta \mathbf{U}^{(k)}.\end{aligned}\quad (26)$$

In eq. 26, the  $A_k$  and  $B_k$  coefficients are functions of the standard Butcher matrix entries,  $\mathbf{R}^{(k)}$  is the residual at the  $k$ -th intermediate RK stage, and  $\mathbf{U}^{(k)}$  is the DoFs vector at the same RK stage. It is important to note that  $\mathbf{U}^{(k)}$ ,  $\Delta \mathbf{U}^{(k)}$  and  $\mathbf{R}^{(k)}$  must be stored, so only three storage registers for each variable are needed for this kind of scheme. This enables us to obtain a good performance in large-scale computations too [24].

We considered ERK schemes having an order of accuracy ranging from 2 to 4; the tables of the coefficients  $A_k$  and  $B_k$  are given below. For the 2nd-order scheme (with 2 stages), named RK 2-2 in the text, we have:

$A_k$	$B_k$
0	1.0
-1.0	0.5

The 3rd-order low-storage ERK scheme (with 4 stages), called RK 3-4 in the paper, is based on the following coefficients proposed by Carpenter and Kennedy [25]:

$A_k$	$B_k$
0	8/141
-756391/934407	6627/2000
-36441873/15625000	609375/1085297
-1953125/1085297	198961/526383

Lastly, a 4th-order accurate approach (with 5 stages) was also adopted, as proposed by Kennedy et al. [24], and called RK 4-5 in our work:

$A_k$	$B_k$
0	0.1496590219993
-0.4178904745	0.3792103129999
-1.192151694643	0.8229550293869
-1.697784692471	0.6994504559488
-1.514183444257	0.1530572479681

### 3.3 Implementation aspects

The solution algorithm is implemented in the OpenFOAM environment [26], which is an open-source library for numerical simulations in continuum mechanics. Thanks to an object-oriented structure, the package is extremely flexible and it allows for outside users to develop complex physical models with relatively little effort.

The basic OpenFOAM classes, *i.e.* `scalarField`, `vectorField` and `tensorField`, have been conceived to mimic the main mathematical tools needed in traditional continuum mechanics. Data type can also be specified in the cells or face centers. We also have two different types of tensor-derivative class: `finiteVolumeCalculus` or `fvc`, and `finiteVolumeMethod` or `fvm`. The former performs explicit estimates of tensorial operators, while the latter can return a matrix representation of a given operation. More details about the above-mentioned data types can be found in [26, 27, 28].

In this paper, we only use the basic classes and the `fvc`-derived class because we opted for an explicit time integration approach. The hyperbolic version of the Eikonal equation was also solved in a fully explicit way using the `fvc` class.

### 3.4 Parallel performance

To investigate the parallel scalability of `caafoam`, we considered a widely-used benchmark, *i.e.* the lid-driven cavity problem of a laminar flow with a low Mach number in a 3D cubic domain [29, 30, 31]. All the boundaries were treated as walls except for the top, which was a moving wall. The strong scaling tests were run on a suite of three evenly-spaced grids with a number of cells  $N_c$  amounting to:  $320^3$ ,  $240^3$  and  $160^3$ . We also set the Reynolds number at 20, and the Mach number relating to the wall velocity at 0.2.

In our specific case, the simulations were conducted on two different super-

computers: MARCONI–A2 hosted by CINECA; and MareNostrum hosted by BSC. MARCONI is a NeXtScale cluster consisting of 3600 nodes with a Knights Landing (KNL) 68-core, 1.40 GHz Intel processor. Each node is equipped with 96 GB of RAM and 16 GB of multi-channel dynamic random access memory (MCDRAM). MareNostrum comprises 3456 nodes with two Intel Xeon Platinum 24-core processors of the Skylake (SKL) generation operating at 2.1 GHz for each node. There are 96 GB of RAM available in standard nodes (as used in this work). Both systems are of the Tier-0 type forming part of the PRACE initiative, [32].

The scalability tests discussed below were conducted as part of a preparatory PRACE project aiming to examine the parallel performance of `caafoam` on massively parallel supercomputers. Access to the machines was limited, so these tests could not be performed using all the solvers considered in this work. Only `caafoam-m1` was therefore considered at this stage because it shares the same spatial discretization approach as standard OpenFOAM solvers.

The tests were conducted without any I/O for 100 time-steps to cancel the starting overhead, and using 64 CPU cores for each MARCONI node, while 48 CPU cores were used for each MareNostrum node. The code was built using Intel compilers and the MPI library version developed by Intel.

Fig. 2 shows the effect of grid size scalability in terms of speed-up and parallel efficiency. It is worth noting that inter-node scalability is good on both systems until the latency due to node communications becomes predominant. It is also very obvious that, on MARCONI, smaller grids have a better parallel performance with fewer cores, while grids with more cells perform better using a larger number of CPU cores. A clearly different trend is apparent on MareNostrum, where performance is almost always super-linear due to cache effects. In this case, smaller grids perform better than larger ones until communications issues override the parallel effects. A super-linear behavior is only achieved on MARCONI up to 2048 CPU cores, using the finest grid, on which we obtain a good parallel performance up to 8192 CPU cores. A good efficiency was achieved on MARCONI up to  $4 \cdot 10^3$  cells for each core, while on MareNostrum we obtained an efficiency of about 88 % with 2250 cells per core.

As concerns the above results, it is important to note that adopting an explicit time integration approach is particularly appealing from the parallel efficiency standpoint. Appropriately selecting the scheme coefficients also enables us to obtain good stability limits, as shown in Section 4.1.1. These are the reasons why we consider `caafoam` an appealing tool for massively parallel aeroacoustic simulations.

## 4 Results

Several literature benchmark problems were considered to test the reliability of the `caafoam` solver. We considered the far-field aerodynamic sound generated

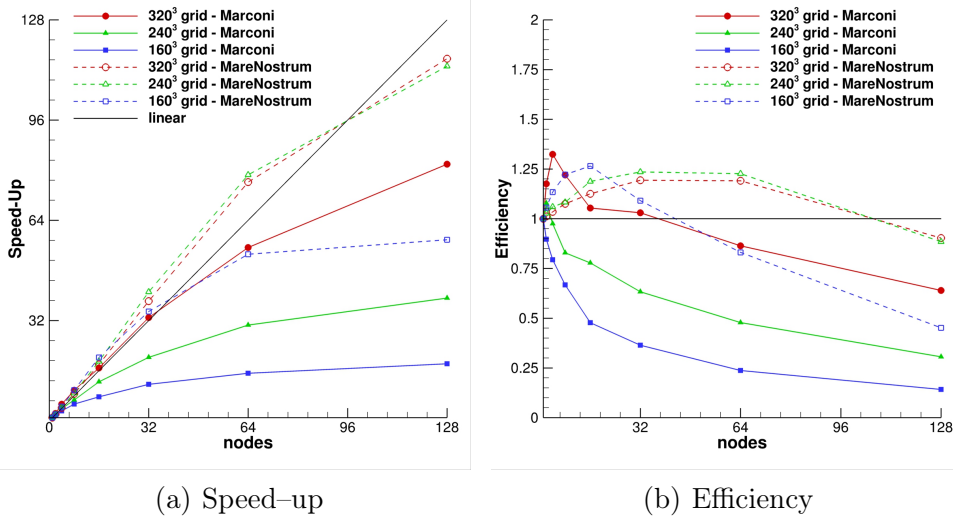


Figure 2. Parallel performance.

by bluff bodies in a flow with a uniform inlet velocity, in various arrangements, at low Mach numbers. The cases of a single circular cylinder and of two square cylinders placed side by side, as well as in a tandem configuration, were analyzed to test the capabilities of our approach. Then a numerical study was conducted on the effect of the wall's thermal boundary conditions on the aeroacoustic field by addressing the sound generated by the flow over isolated square and circular cylinders.

In all the above-mentioned cases, the Mach number of the undisturbed flow was  $M_\infty = 0.2$ ,  $\gamma = 1.4$ , and the Prandtl number,  $\text{Pr}$ , was 0.75. We present the results below in terms of standard parameters relating to fluid dynamic and acoustic fields, i.e. (i) drag and lift coefficients; (ii) the Strouhal number; (iii) fluctuations in pressure and its root mean square; and (iv) dilatation rate field. The dimensionless drag and lift coefficients are given by eq. 27:

$$C_D = \frac{2D'}{\rho u_\infty^2 A_{ref}}, \quad C_L = \frac{2L'}{\rho u_\infty^2 A_{ref}}. \quad (27)$$

Standard statistics are used to analyze force coefficients behavior: the mean drag coefficient  $\langle C_D \rangle$ , the root mean square of the lift coefficient  $C_{L,rms}$ , and the amplitudes of oscillation of the force coefficients ( $\Delta C_D = (C_{D,max} - C_{D,min})/2$ , and  $\Delta C_L = (C_{L,max} - C_{L,min})/2$ ). The Strouhal number is defined as:

$$\text{St} = \frac{f L_{ref}}{u_\infty} \quad (28)$$

where  $f$  is the vortex-shedding frequency found from spectral analysis of the time history of the fluctuating lift coefficient, and  $L_{ref}$  is the reference length. The acoustic results are presented below in terms of dimensionless fluctuating pressure, defined as:

$$p' = \frac{p - \langle p \rangle}{\rho_\infty c_\infty^2} \quad (29)$$

where  $\langle p \rangle$  is the average pressure field and  $c_\infty$  is the speed of sound of the undisturbed flow. Polar plots containing the root mean square of  $p'$  are shown to elucidate the sound features in the far field. For the purpose of a comparison with the literature, the acoustic statistics were sampled over a dimensionless time  $u_\infty T/D = 100$ . Unless stated otherwise, the plots are built at  $r/D = 75$ . The dilatation rate field,  $\partial u_j / \partial x_j$ , is also used to visualize the acoustic wave because, taking the mass conservation equation into account, it equates to the negative rate of change of the density which is directly linked to  $p'$ .

Finally, the acoustic power output, defined as the acoustic intensity flux through a closed circle surrounding the source and having a radius  $r'$ , is examined to estimate the wall heating effects on the sound produced. The analytical expression of the acoustic power is as follows:

$$W = \int_0^{2\pi} I_a(r = r', \theta) R d\theta \quad (30)$$

where  $I_a = (p'_{rms})^2 / \rho c$  accounts for the mean acoustic intensity in the far-field region. The sound power level is obtained as:

$$L_w = 10 \log_{10} \frac{W}{W_0} \quad (31)$$

where  $W_0$  is the reference acoustic power.

All the solutions were obtained on distributed-memory parallel machines: the computations requiring a lower load were run on a Linux Cluster, with 16 Intel Xeon E5-2603v3-based nodes, for a total of 192 CPU cores operating at 1.6 GHz. Larger cases were run on a MARCONI-A2 system. Intel's `libhbm` library, which can be downloaded from the OpenFOAM-dev-Intel branch on Github (<https://github.com/OpenFOAM/OpenFOAM-Intel/tree/master/libhbm>), was used to enable access to the MCDRAM. Adopting `libhbm` enabled us to speed up the computations by up to 20%.

#### 4.1 Validation cases

##### 4.1.1 Circular cylinder

The first test case in this work concerns the sound generated by the Karman vortex street that is shed behind a circular cylinder. The Reynolds number based on the cylinder's diameter is  $Re = 150$ . The problem had already been considered in the context of sound generation computation [33, 34, 35, 36], so it is an appropriate benchmark for `caaf foam`.

Two different suites of computational meshes were generated to test the performance of `caaf foam`. A first group included three fully-structured O-type grids. The coarser structured grid, named G1, was created with  $N_c = 3.5 \cdot 10^5$  ( $500 \times 700$ ); the G2 grid was generated by starting from G1 and increasing the num-

ber of cells in the radial direction,  $N_c = 5.25 \cdot 10^5$  ( $750 \times 700$ ). The last grid, G3, was the result of a further refinement in the radial direction:  $N_c = 7 \cdot 10^5$  ( $1000 \times 700$ ). It is important to remark that the G series grids have a number of cells per wavelength equal to about: 90 for G1, 135 for G2 and 180 for G3. Note also that the previous data are compatible with recent literature references [36, 37, 38]. Our second set of computational meshes consisted of two fully-unstructured (triangular cells) grids: the U2 grid had about  $2 \cdot 10^6$  cells and was obtained by refining a starting grid, named U1 with  $N_c \simeq 5.2 \cdot 10^5$ , in order to have a wavelength resolution comparable to G2 grid. In all the above cases, the far-field boundaries were placed at 150 times the cylinder's diameter,  $D$ , and the height of the first cell next to the wall,  $y_c$ , was set at  $y_c/D = 5 \cdot 10^{-3}$ . The sponge's strength was set at 40 dB. The different space discretized domains were tested using both versions of `caafoam`, i.e. `m1` and `m2`.

An instantaneous representation of the pressure wave generated by vortex shedding, computed with our low-dissipation approach, is shown in Fig. 3. It contains the positive and negative pressure pulses, alternately produced from the upper and lower sides of the cylinder, as also noted by Inoue and Hatakeyama, [34].

Fig. 4 shows the polar plots of the root mean square of the fluctuating pres-

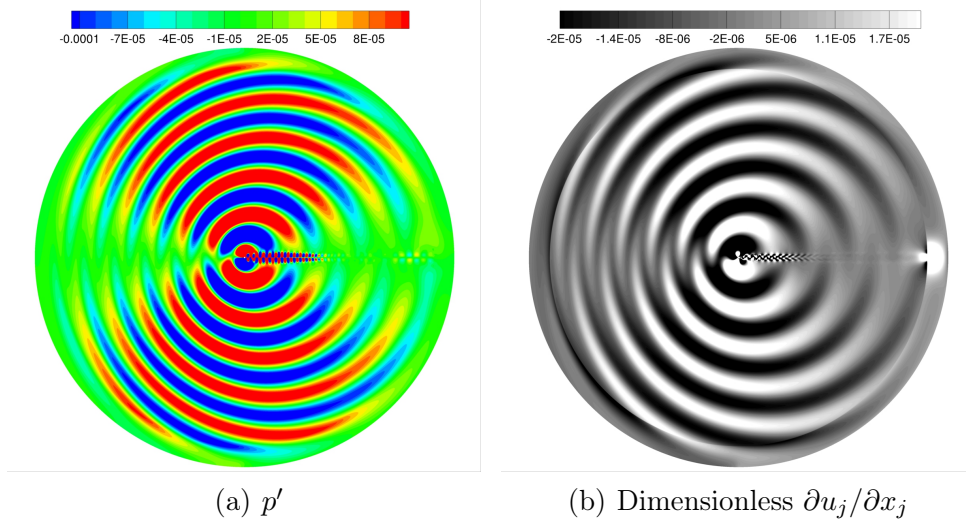


Figure 3. Sound wave generated by the flow past a circular cylinder at  $Re = 150$ .

sure,  $p'_{rms}$ , obtained using the RK 4-5 scheme and the maximum allowable Co number. The nature of the sound field clearly emerges, also confirming that the lift dipole dominates. Fig. 4(a) clearly shows that good reconstruction of the acoustic far field can be obtained with the G2 grid. In fact, solutions G2 and G3 are almost indistinguishable, while some little wiggles appear for in the case of G1. It is important to note that `caafoam-m1` and `caafoam-m2` (without the dissipative term on the pressure flux, *i.e.*  $\alpha = 0$ ) produce very similar results on the structured grids. On the other hand, `caafoam-m1` proved unstable on our unstructured grids without any limiters on the interpolation schemes

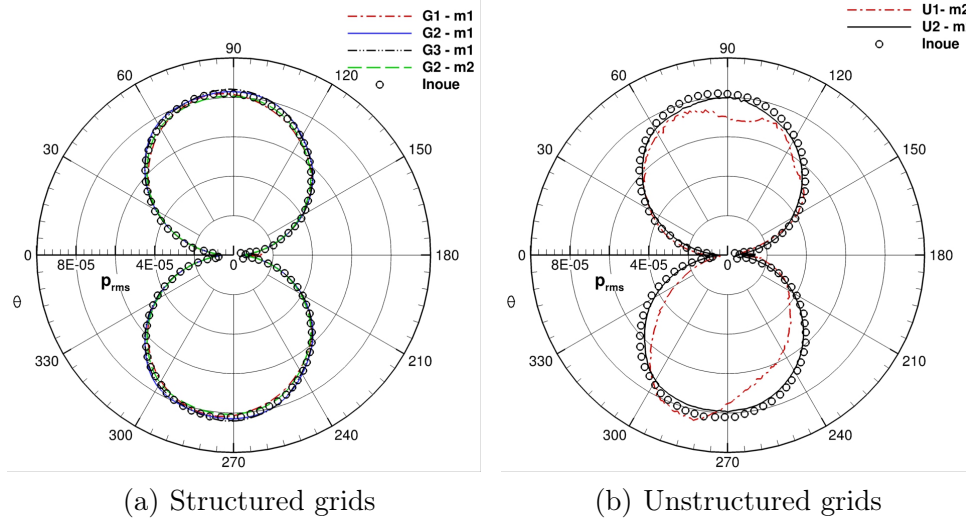


Figure 4. Flow past a circular cylinder at  $Re = 150$ . Grids effect.

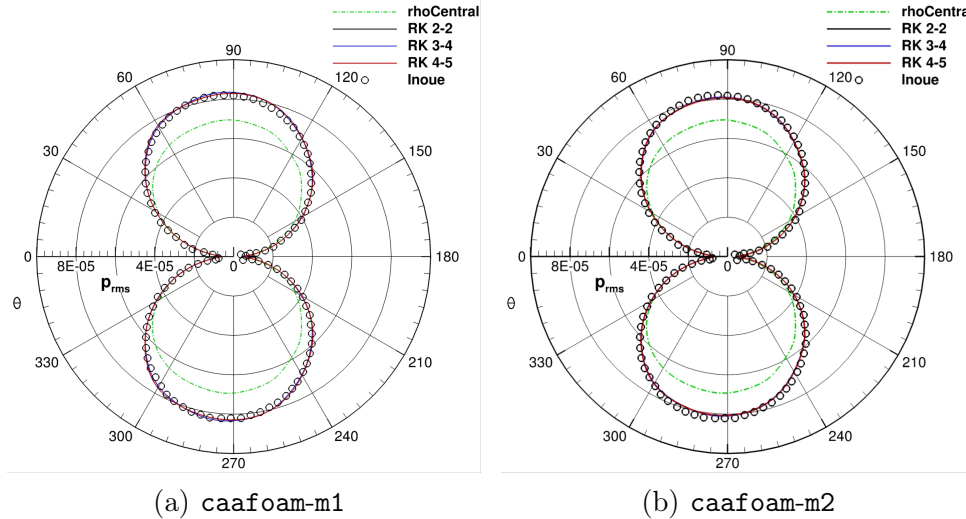


Figure 5. Flow past a circular cylinder at  $Re = 150$ . G2 grid. RK scheme effect;  $Co_{max} \approx 0.2$ .

for the DoFs, which in turn cause acoustic wave depletion. Only `caafoam-m2` with  $\alpha = 1$  proved capable of directly simulating the acoustic field on the U1 and U2 grids (see Fig. 4(b)). The main drawback of adopting unstructured grids, however, lies in the dramatic increase in the number of cells needed to obtain acceptable predictions. Our investigations were consequently limited to structured meshes from this point on.

Fig. 5 is worthy of careful attention because it shows the comparison (performed on the G2 grid) between our approach and the results obtained with `rhoCentralFoam`. The solver is density-based and available in the official OpenFOAM release. It adopts the KNP scheme for the space discretization of the convective terms [16]. In this particular case, `rhoCentralFoam` was submitted to the non-reflective boundary treatment described in Section 2.1. Fig. 5

shows that `rhoCentralFoam` is unable to properly reconstruct the acoustic field. This is due to the significant amount of numerical dissipation introduced by the solver, as also noted by Modesti and Pirozzoli [20] in a different context. We might also add that the “backward” scheme, available in the official OpenFOAM releases, was used in `rhoCentralFoam` for time integration. The RK-based approaches proposed in this work show a very good agreement with the reference data in both `caafoam-m1` and `caafoam-m2` modes (see Fig. 4). They also show a directivity of  $83^\circ$ , which differs from Inoue and Hatakeyama, who found  $78.5^\circ$ , by 5.7%. We can therefore conclude that, on structured grids, the space discretization needed to handle Eulerian numerical fluxes is not the crucial issue. Our results demonstrate that, in the FV framework, the solution strategy of space discretized equations has a central role in the correct prediction of acoustic waves. For the sake of completeness, we must add that applying `rhoCentralFoam` to unstructured grids suffers from the same problems as those described for `caafoam-m1`, which also use the KNP approach. In our computational experience, we found that a  $Co_{max}$  of about 1 can be used when the RK 4-5 technique was adopted. The RK 3-4 scheme only proved stable for  $Co_{max} \approx 0.6$ , whereas for RK 2-2 the maximum allowable Courant number was around 0.4. Fig. 5 suggests that the RK 2-2 approach is the best choice for solving the governing equations because, in both `m1` and `m2` modes, it enables us to obtain results comparable with the RK 3-4 and RK 4-5 schemes using only 2 stages. We have to emphasize, however, that the RK 2-2 and RK 4-5 schemes are less costly because they have the same ratio between the number of computational operations and the stability limits. In the following cases, we preferred to adopt the RK 4-5 technique because it provided slightly better results than the RK 2-2 method. As shown in Fig. 6,

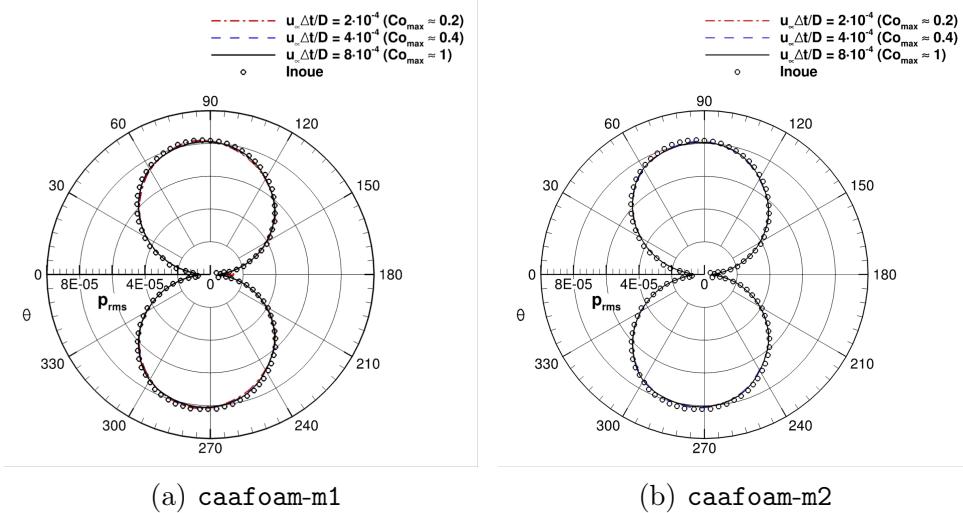


Figure 6. Flow past a circular cylinder at  $Re = 150$ . G2 grid. Time-step size effect.

the increase in the size of the  $\Delta t$  does not significantly affect the accuracy of the solution for either of the schemes for approximating the convective terms considered in this paper.

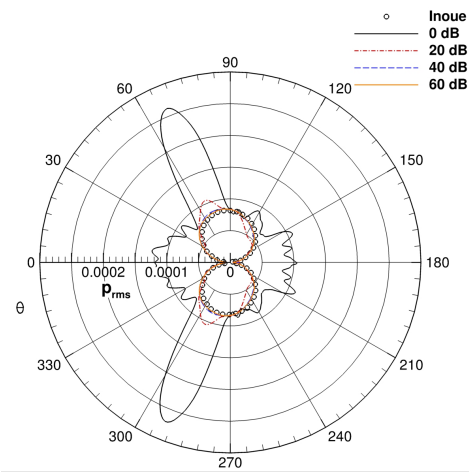


Figure 7. Flow past a circular cylinder at  $\text{Re} = 150$ . G2 grid. Sponge layer strength impact.

Finally, we wish to confirm that a non-reflective boundary treatment is indispensable for DNS cases. Sponge-layer-free numerical solutions produce completely nonphysical results (see Fig. 7). A sponge strength of 40 dB suffices, as also noted by Mani [13], to properly suppress spurious wave reflections near the boundary field. The sponge layer thickness was computed using the criterion discussed in Section 2.1.

Table 1 and Table 2 show the aerodynamic parameters regarding the effect of the time-step's size, including the `rhoCentralFoam` solutions. The maximum dimensionless time-step size,  $u_\infty \Delta t / D$ , was chosen in order to overcome the stability limit of the scheme considered. For `rhoCentralFoam`,  $\text{Co}_{max}$  has to be less than 0.2 to avoid the computation blowing up. For the sake of compactness, the above-mentioned results only refer to the G2 grid, and they almost converge. The force coefficients established with `caafoam` are very consistent with the results reported by Inoue and Hatakeyama [34], and by Muller [33] high-order finite difference data (see Table 3). The Strouhal number was also computed, obtaining  $\text{St} = 0.182$  for all the cases considered. Here again, our results are very consistent with the main references in the literature. Compared with `caafoam`, the `rhoCentralFoam` solver slightly overestimates the amplitudes of the aerodynamic coefficients, but it has a good overall fit with the data in the literature.

#### 4.1.2 Square cylinders arranged side by side: $L/D = 3$

In this subsection we discuss the results concerning the flow field and sound generation around two square cylinders placed side by side, as shown in Fig. 8. The ratio  $L/D$  was set at 3, where  $L$  is the spacing between the centers of the two cylinders and  $D$  is the diameter. The Reynolds number, based on a single cylinder's diameter, is  $\text{Re} = 150$ . Depending on the initial condition, a bifurcation of the wake patterns appears for this flow configuration, as for

Table 1

Cylinder at  $\text{Re} = 150$ ,  $M_\infty = 0.2$ , G2-grid results. `caafoam-m1`

Case	$u_\infty \Delta t/D$	$\langle C_D \rangle$	$\Delta C_D \cdot 10^2$	$\Delta C_L$	St
RK 2–2 ( $\text{Co}_{max} \simeq 0.2$ )	$2 \cdot 10^{-4}$	1.3326	2.580	0.5203	0.182
RK 2–2 ( $\text{Co}_{max} \simeq 0.4$ )	$4 \cdot 10^{-4}$	1.3325	2.560	0.5200	0.182
RK 3–4 ( $\text{Co}_{max} \simeq 0.2$ )	$2 \cdot 10^{-4}$	1.3329	2.570	0.5203	0.182
RK 3–4 ( $\text{Co}_{max} \simeq 0.4$ )	$4 \cdot 10^{-4}$	1.3329	2.575	0.5201	0.182
RK 3–4 ( $\text{Co}_{max} \simeq 0.6$ )	$6 \cdot 10^{-4}$	1.3325	2.580	0.5199	0.182
RK 4–5 ( $\text{Co}_{max} \simeq 0.2$ )	$2 \cdot 10^{-4}$	1.3329	2.580	0.5203	0.182
RK 4–5 ( $\text{Co}_{max} \simeq 0.4$ )	$4 \cdot 10^{-4}$	1.3328	2.575	0.5201	0.182
RK 4–5 ( $\text{Co}_{max} \simeq 1.0$ )	$8 \cdot 10^{-4}$	1.3325	2.570	0.5199	0.182
<code>rhoCentralFoam</code> ( $\text{Co}_{max} \simeq 0.2$ )	$2 \cdot 10^{-4}$	1.3347	2.580	0.5215	0.182

Table 2

Cylinder at  $\text{Re} = 150$ ,  $M_\infty = 0.2$ , G2-grid results. `caafoam-m2`

Case	$u_\infty \Delta t/D$	$\langle C_D \rangle$	$\Delta C_D \cdot 10^2$	$\Delta C_L$	St
RK 2–2 ( $\text{Co}_{max} \simeq 0.2$ )	$2 \cdot 10^{-4}$	1.3321	2.565	0.5183	0.182
RK 2–2 ( $\text{Co}_{max} \simeq 0.4$ )	$4 \cdot 10^{-4}$	1.3321	2.565	0.5183	0.182
RK 3–4 ( $\text{Co}_{max} \simeq 0.2$ )	$2 \cdot 10^{-4}$	1.3321	2.565	0.5183	0.182
RK 3–4 ( $\text{Co}_{max} \simeq 0.4$ )	$4 \cdot 10^{-4}$	1.3321	2.566	0.5183	0.182
RK 3–4 ( $\text{Co}_{max} \simeq 0.6$ )	$6 \cdot 10^{-4}$	1.3321	2.564	0.5183	0.183
RK 4–5 ( $\text{Co}_{max} \simeq 0.2$ )	$2 \cdot 10^{-4}$	1.3321	2.564	0.5183	0.182
RK 4–5 ( $\text{Co}_{max} \simeq 0.4$ )	$4 \cdot 10^{-4}$	1.3347	2.565	0.5182	0.182
RK 4–5 ( $\text{Co}_{max} \simeq 1.0$ )	$8 \cdot 10^{-4}$	1.3321	2.564	0.5183	0.182
<code>rhoCentralFoam</code> ( $\text{Co}_{max} \simeq 0.2$ )	$2 \cdot 10^{-4}$	1.3347	2.580	0.5215	0.182

Table 3

Cylinder at  $\text{Re} = 150$ . Literature data.

Case	$\langle C_D \rangle$	$\Delta C_D \cdot 10^2$	$\Delta C_L$	St
Muller [33]	1.34	2.6	0.52	0.183
Inoue and Hakateyama [34]	1.32	2.6	0.52	0.183
Williamson [47] (Exp.)	—	—	—	0.18

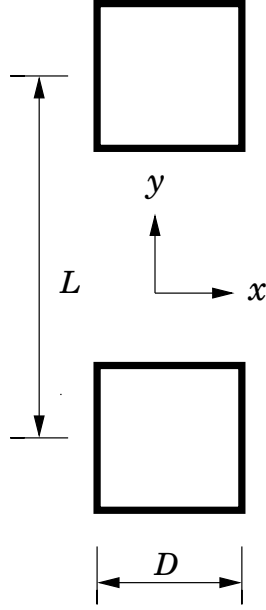
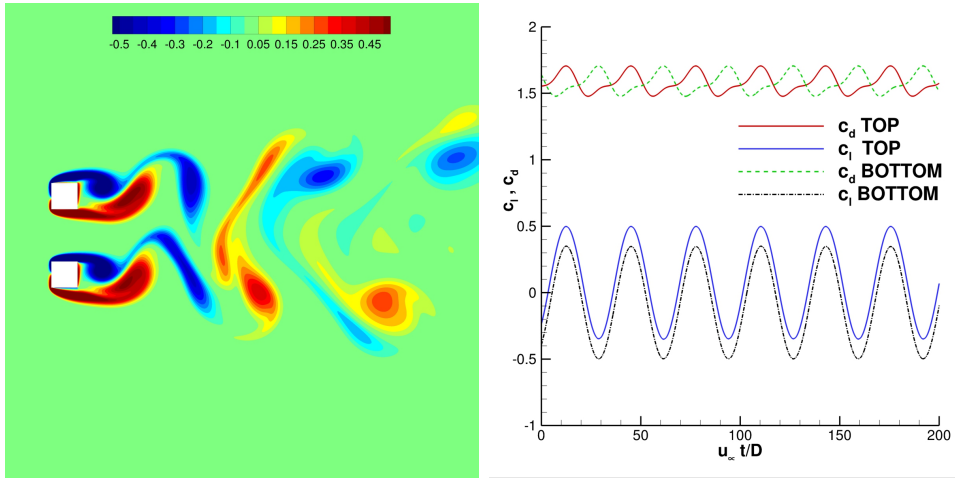


Figure 8. Cylinders arranged side by side.

circular cylinders [39]. Different sound patterns are generated in response to this phenomenon [40]. In this work, a symmetrical initial field (with respect to the  $y = 0$  plane) was imposed by two vortices, one moving clockwise and the other counterclockwise, behind the upper and lower cylinders, respectively. The resulting flow field is described as in-phase because it exhibits synchronized lift coefficients (Fig. 9(b)). Fully-structured orthogonal computational



(a) Dimensionless vorticity field

(b) Force coefficients time history

Figure 9. Square cylinders side by side at  $\text{Re} = 150$ ,  $M_\infty = 0.2$ ,  $L/D = 3$ . Finer grid results.

grids were used, adopting a sponge layer with a strength of 40 dB. The grid cells were clustered near the cylinder walls, whereas the far field was placed at  $200 D$  from the midpoint of the two cylinders (see Fig. 8).  $N_c$  was set at  $1.11 \cdot 10^6$ . It should be noted that we had to extend the domain due to the

lower frequency of vortices shed behind the square cylinders than behind the single circular one. For this reason,  $L_{sp}$  was increased to keep the dimensionless extent of the sponge layer,  $L_{sp}f/c_\infty$ , at 0.5. The inflow/outflow conditions were consequently set at  $200 D$  to avoid interference phenomena between the acoustic far field and the layer. A finer version of the grid was also generated: it has a number of cells equating to half that of the previous grid, with a total number of  $4.44 \cdot 10^6$ , and the height of the dimensionless first cell bordering on the walls is  $10^{-2}$ . Note that the finest grid guarantees about 180 cells per wavelength. Time integration was performed using the RK 4-5 scheme and the size of the dimensionless time step was set at  $1.8 \cdot 10^{-3}$ . This enabled us to obtain a maximum Courant number of around 1 for the finer grid. The larger case was run on the MARCONI-A2 system using 256 CPU cores.

The main aims of this benchmark are to further validate `caafoam`, and also to investigate the role of the solution strategy involving space-discretized equations in the context of the structured grids. We consequently limit our efforts to the `m1` version of our code because it uses the same space discretization approach as `rhoCentralFoam`, and it is equivalent to `m2` in terms of the results on structured grids.

Table 4 shows the aerodynamic parameters predicted from the above-mentioned computations. An overall good agreement emerged between our data and those in the literature. We might also add that it is hard to say whether the intrinsically dissipative nature of `rhoCentralFoam` could affect the forces predicted. Finally, Fig. 10 shows the acoustic results. The overall results show a good agreement with the findings of Inoue et al. [40], but our grid refinement clearly improved the agreement between the data presented here and those in the literature. Fig. 10(a) shows the  $p'_{rms}$  polar plot, which is very similar to the case of the single circular cylinder: a directivity of  $80.2^\circ$  was obtained. It is important to note that the sound wave is always symmetrical to the  $y = 0$  plane, and of a similar nature to the longitudinal quadrupole, as discussed in Blake [41]. Once again, the non-reflective `rhoCentralFoam` version does not properly reconstruct the acoustic far field, as shown in Fig. 10.

This confirms that, here too, the space discretization schemes adopted for the governing equations are not the main factor responsible for correctly predicting acoustic waves.

#### 4.1.3 Square cylinders in tandem: $L/D = 2$

With the same aims as for the side-by-side arrangement, we also considered the flow and sound generation around two square cylinders in a tandem configuration with  $L/D = 2$ , where  $L$  and  $D$  have the meaning expressed in Fig. 11.

The computational domain was generated to place the far field  $200 D$  away from the origin of the Cartesian frame in Fig. 11. Quadrilateral orthogonal cells were used to discretize the flow domain. The total number of cells,  $N_c$ , was about  $4.2 \cdot 10^6$ , and a grid refinement was performed near the walls of

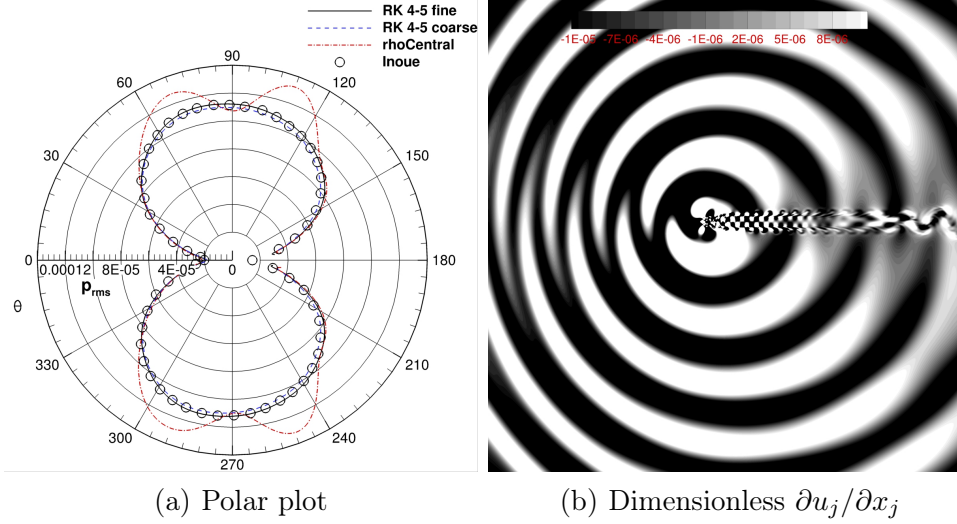


Figure 10. Square cylinders side by side at  $Re = 150$ ,  $M_\infty = 0.2$ ,  $L/D = 3$ .

Table 4

Side-by-side square cylinders at  $Re = 150$ ,  $M_\infty = 0.2$ . Force coefficients.

	RK 4-5 coarse	RK 4-5 fine	rhoCentralFoam (fine)	Inoue [40]
$\langle C_D \rangle$	1.5806	1.5920	1.5859	1.5519
$\langle C_L \rangle$	$\pm 0.0759$	$\pm 0.0753$	$\pm 0.0749$	$\pm 0.0689$
$2\Delta C_D$	0.2216	0.2282	0.2281	0.2377
$2\Delta C_L$	0.8286	0.8479	0.8456	0.8575
St	0.153	0.144	0.155	0.150

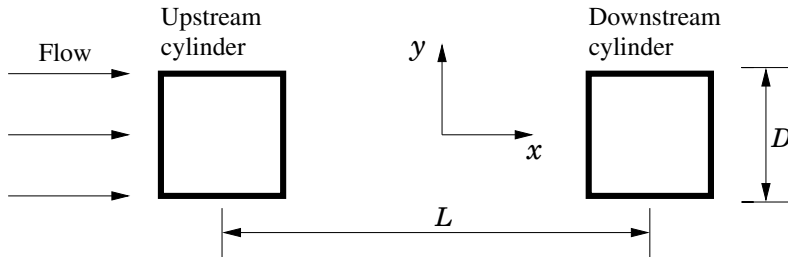


Figure 11. Square cylinders in tandem configuration.

the cylinders adopting  $y_c/D = 10^{-2}$ . This grid allows to have about 190 cells per wavelength for the specific configuration. As for the side-by-side configuration, we tested a coarser grid with a quarter of the  $N_c$  of the finer one. The `caaf foam-m1` solutions are based on the RK 4-5 time integration scheme to obtain a maximum allowable Courant number of around 1. So  $u_\infty \Delta t / D$  was set at  $9 \cdot 10^{-3}$  for the finer grid. Acoustic wave reflections at the far boundaries were removed using a configuration derived from the previous test cases; the

Table 5

Square cylinder in tandem configuration at  $\text{Re} = 150$ ,  $M_\infty = 0.2$ . Force coefficients.*Upstream cylinder*

Case	$\langle C_D \rangle$	$2\Delta C_D \cdot 10^4$	$2\Delta C_L$	St
RK 4-5 coarse	1.2753	2.0	0.0378	0.134
RK 4-5 fine	1.2803	2.1	0.0384	0.134
<code>rhoCentralFoam</code> (fine)	1.2805	2.1	0.0383	0.134
Inoue et al. [42]	1.2794	—	—	0.133

*Downstream cylinder*

Case	$\langle C_D \rangle$	$2\Delta C_D \cdot 10^3$	$2\Delta C_L$	St
RK 4-5 coarse	-0.1936	1.50	0.106	0.134
RK 4-5 fine	-0.1959	1.54	0.1068	0.134
<code>rhoCentralFoam</code> (fine)	-0.1961	1.53	0.1065	0.134
Inoue et al. [42]	-0.1945	—	—	0.133

sponge layer's strength was 40 dB, while its dimensionless thickness was 0.5 to limit the computational resources required. Finer grid computations were run using 256 CPU-cores MARCONI-A2 HPC system.

Table 5 shows the aerodynamic parameters for the square cylinders in tandem. The picture is similar to the one seen for the side-by-side cylinders. The features of the sound field generated by the interaction of the flow and the two cylinders are shown in Fig. 12. The  $p'_{rms}$  plot in Fig. 12(a) refers to a circle having a  $r/D$  of 80. `caafoam-m1` results, achieved with the finer grid, are consistent with the reference data in the literature [42], and reveal a directivity of  $71.2^\circ$ . Lastly, we wish to add that, for this test case too, the non-reflective `rhoCentralFoam` is inappropriate for far-field sound computation. Fig. 12(a) clearly shows that, in the far zone of the acoustic field, `rhoCentralFoam` is not consistent with the data reported in [42].

#### 4.2 Thermal effects on the aeroacoustic field

Two different configurations were considered to analyze the effect of the thermal boundary conditions at the wall on the acoustic field generated by the laminar flows around bluff bodies: a single circular cylinder at  $\text{Re} = 150$ , and a single square cylinder at the same  $\text{Re}$  number. In both problems, the baseline configuration involved an adiabatic wall; then cases having  $T_w = 2T_\infty$  and  $T_w = 3T_\infty$  were also investigated.  $M_\infty = 0.2$  was used to conduct this

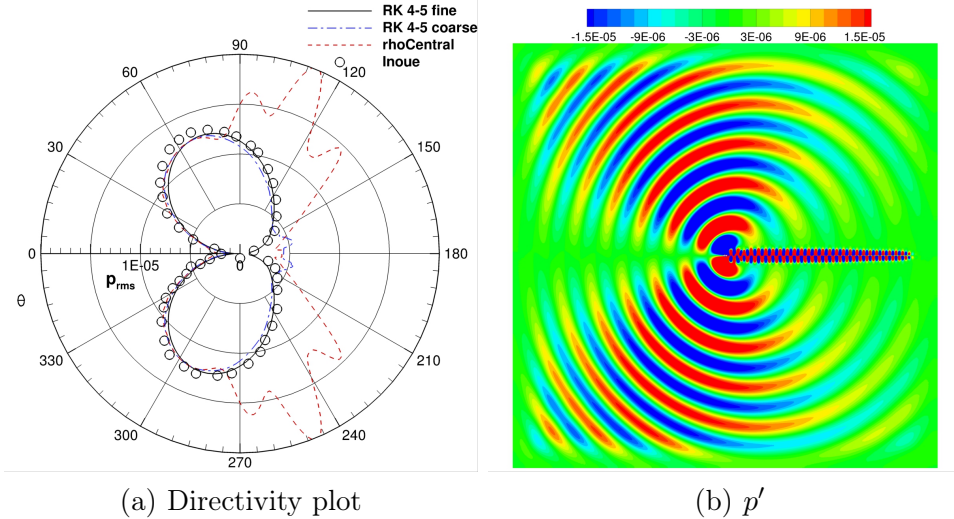


Figure 12. Square cylinders in tandem at  $\text{Re} = 150$ ,  $M_\infty = 0.2$ ,  $L/D = 2$ .

assessment. Given the results presented in the previous sections, the following data were based on `caaf foam-m1`.

The first case we mention, represented in Fig. 13, is the sound radiated by the Karman vortex street shed behind a square cylinder. A fully-structured orthogonal grid was used: the grid cells were clustered near the cylinder walls using a dimensionless first cell height,  $y_c/D$ , of  $5 \cdot 10^{-3}$ , and far-field boundaries placed at a distance of  $200 D$  from the center of the cylinder. The resulting computational mesh had a total number of cells,  $N_c$ , amounting to  $4.4 \cdot 10^6$  with about 170 cells per wavelength. The polar plot containing the  $p'_{rms}$  is shown in Fig. 16(a). The data were collected over a circumference built around the square cylinder having a dimensionless radius  $r/D = 75$ , as in Inoue et al. [42]. Our approach clearly ensures a good reconstruction of the acoustic far field. It is important to note that, for the flow regimes considered, the acoustic field is generated by periodical vortical structures shedding. This phenomenon causes a pressure fluctuation on the cylinder's surfaces, leading to the generation an unsteady lift/downforce. The drag is influenced by the Karman vortex street as well, showing a downstream/upstream pulsation. These perturbations have a sound quadrupole nature, but the dominance of the lift fluctuation yields a typical dipolar acoustic field [43].

Note that, due to thermal effects, in order to estimate the changes in the acoustic field we present our data on a circle having  $r = 40 D$  as this prevents an excessive sound wave decay in the far field. This condition enabled us to set the extent of the computational domain at  $r = 150 D$ , reducing the number of cells to:  $N_c \simeq 3 \cdot 10^6$ . Fig. 14 shows that the rise in wall temperature increases  $\langle C_D \rangle$  and reduces  $C_{L,rms}$ . Fig. 15 shows that the force coefficient pulsations,  $\Delta C_D$  and  $\Delta C_L$ , are reduced as a result of the increase in wall temperature. These results are in agreement with the reports from Lecordier et al. [8, 9], who experimentally found vortex shedding dumping behind a heated circular cylinder. Similar effects were also found on heated airfoils operating at low

$\text{Re}$ , [44, 45, 46], which revealed a higher drag force and lower lift force in steady conditions. Looking at the results in Fig. 15, it is easy to see that the sound sources, *i.e.*  $\Delta C_D$  and  $\Delta C_L$ , are damped, producing a far-field sound abatement at higher wall temperatures. It is worth noting that this phenomenon is not limited to a specific  $\text{Re}$  but holds throughout the range of 90-150, as shown in the figures from Fig. 16 to Fig. 19. The radiated sound decay is also less significant for higher  $\text{Re}$  numbers, as shown in Fig. 20(b). In particular, at  $\text{Re} = 90$  the maximum sound power level decay ( $T_w = 3T_\infty$ ) is slightly less than 5 dB, while at  $\text{Re} = 150$  it is  $\sim 3$  dB, which is still significant. The St number is reduced by wall heating as well, as shown in Fig. 20(a), consistently with the findings of Lecordier et al..

The second case considered in this context is the sound radiated by the Kar-

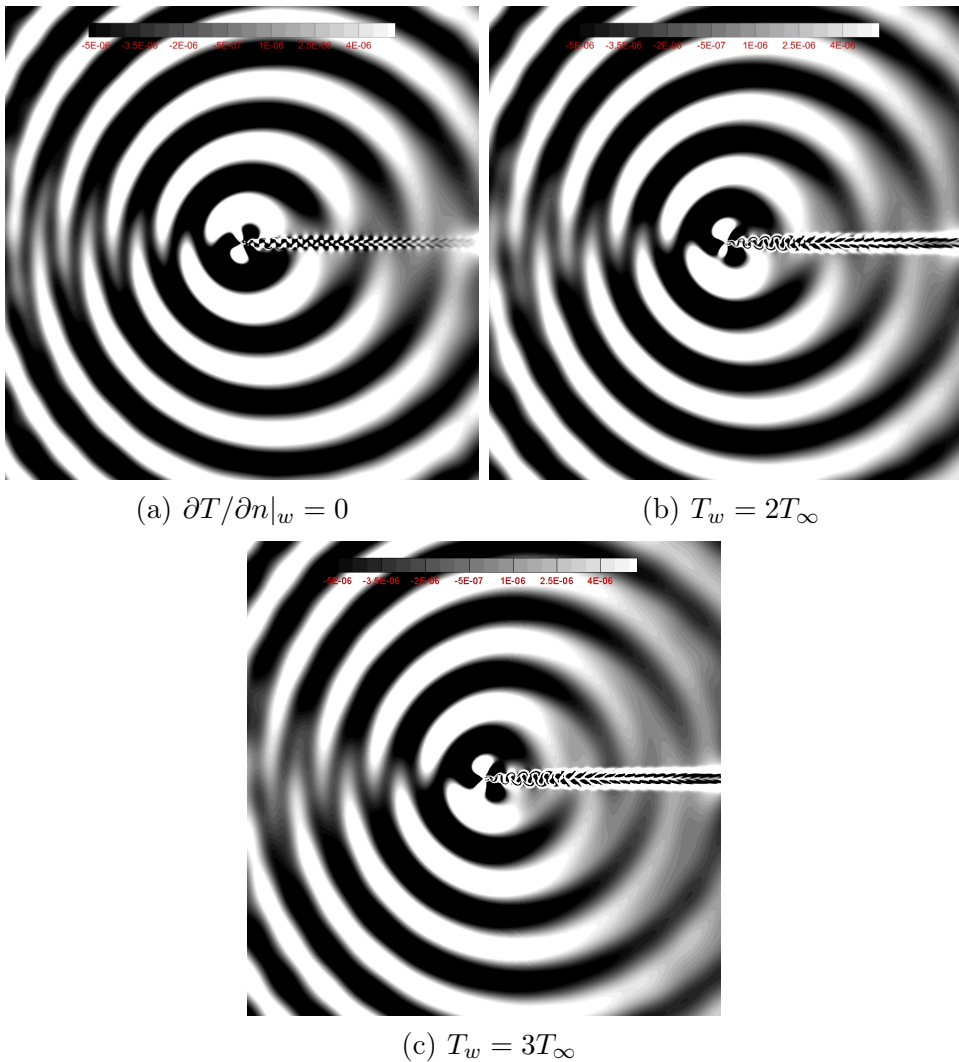


Figure 13. Wall temperature effect, square cylinder  $\text{Re} = 150$ . Dimensionless  $\partial u_j / \partial x_j$ .

man vortex street that is shed behind a circular cylinder. The fully-structured G2 grid was used for this analysis. All the numerical settings mentioned in

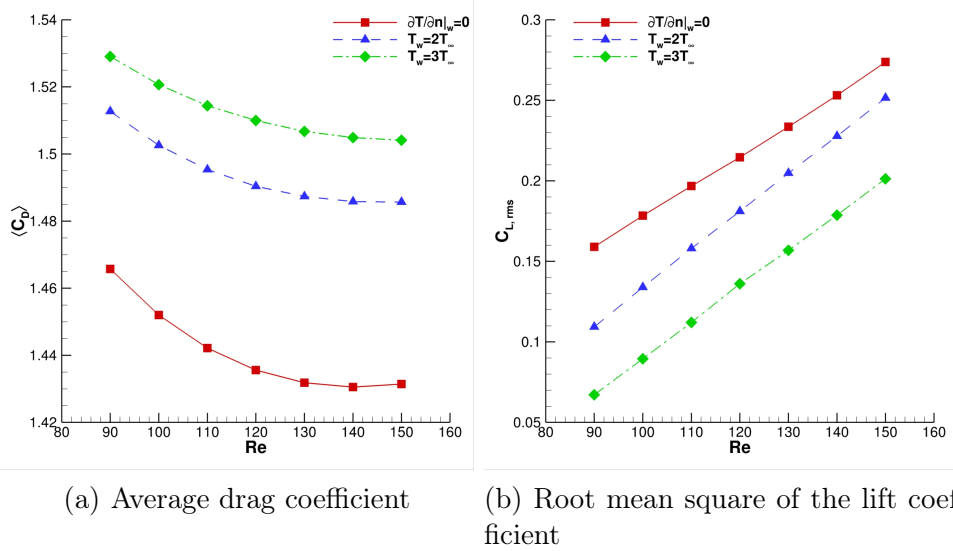


Figure 14. Wall temperature effect, square cylinders. Force coefficients.

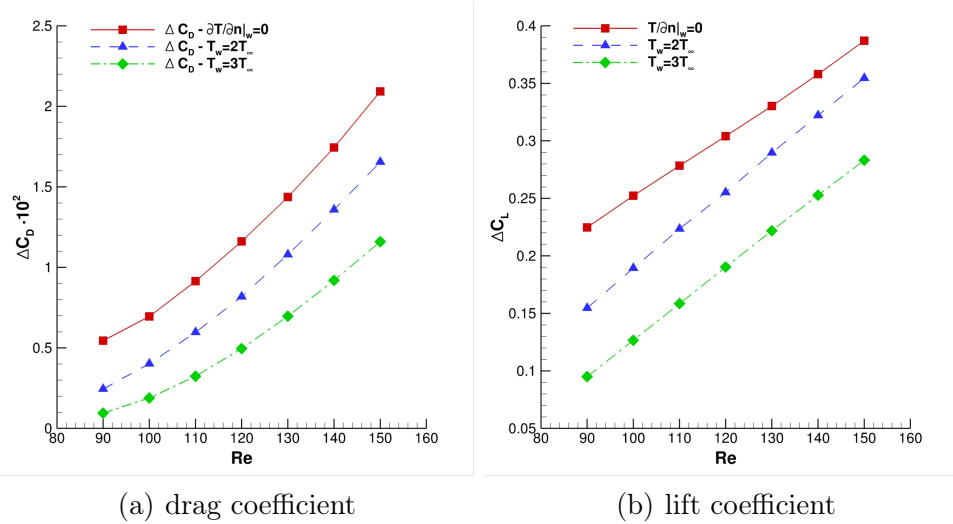


Figure 15. Wall temperature effect, square cylinders. Force coefficients fluctuations.

Section 4.1.1 were confirmed here to investigate the effects of wall heating on the radiated sound. As for the square cylinder, we present the  $p'_{rms}$  data on a circle having  $r = 40 D$ .

In this case, increasing the wall temperature produced an evident reduction in  $C_{L,rms}$ , while  $\langle C_D \rangle$  was increased up to  $Re = 130$ . Fig. 21 clearly shows, however, that the thermal boundary conditions at the wall have a more significant effect on the lift coefficient in this flow configuration, whereas the effect on  $\langle C_D \rangle$  is almost negligible. As for the square cylinder, the force coefficient fluctuations are dumped.

In short, the aeroacoustic sound emitted in the far-field region is lower when the wall temperature is higher, as shown in Fig. 23 to Fig. 26. It is also important to note that the sound decay is less significant at higher Re numbers

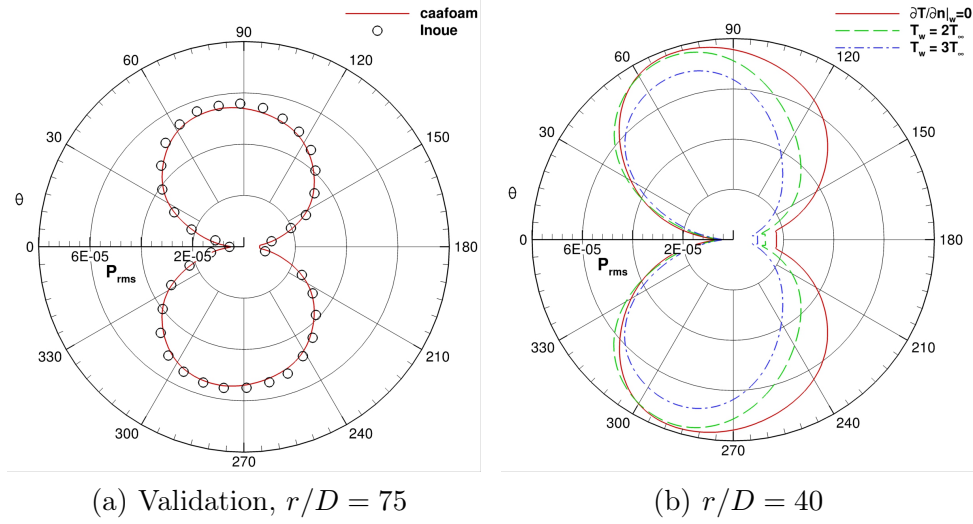


Figure 16. Wall temperature effect, square cylinder at  $\text{Re} = 150$ .

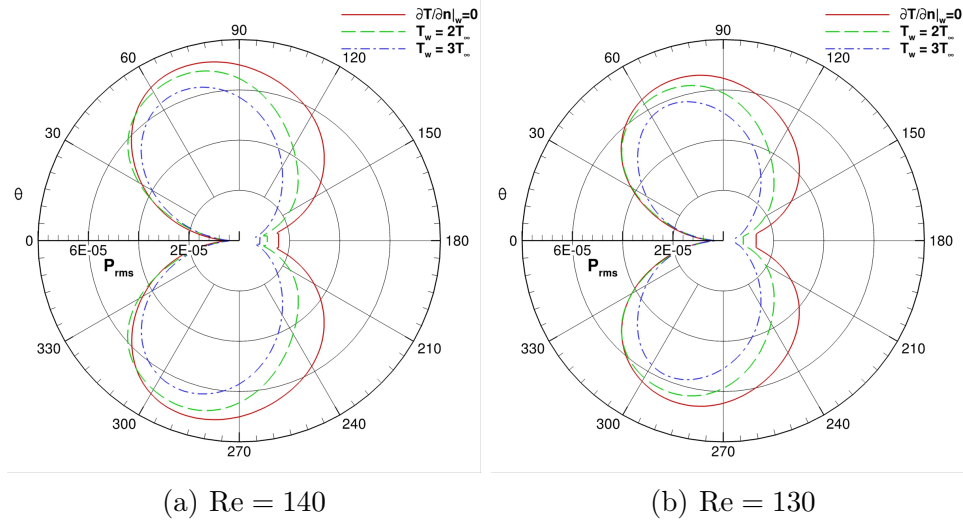


Figure 17. Wall temperature effect, square cylinder.  $p'_{rms}$ ,  $r/D = 40$ .

in this configuration, as confirmed by Fig. 27(b). It is also worth noting that overall  $L_w$  abatement is greater for the circular cylinder than for the square one. In fact, we obtained  $\Delta L_w \simeq 8\text{dB}$  at  $\text{Re} = 90$ , and  $\sim 5\text{dB}$  at  $\text{Re} = 150$ . Lastly, the St number shows the same behavior vis-à-vis  $\text{Re}$  and wall temperature as for the square cylinder.

At the time of writing this paper, there were no papers available in the open literature dealing with the reduction of emitted aeroacoustic sound based on wall heating. The above-mentioned phenomenon was analyzed on two completely different geometries, showing that it is not limited to a particular flow configuration.

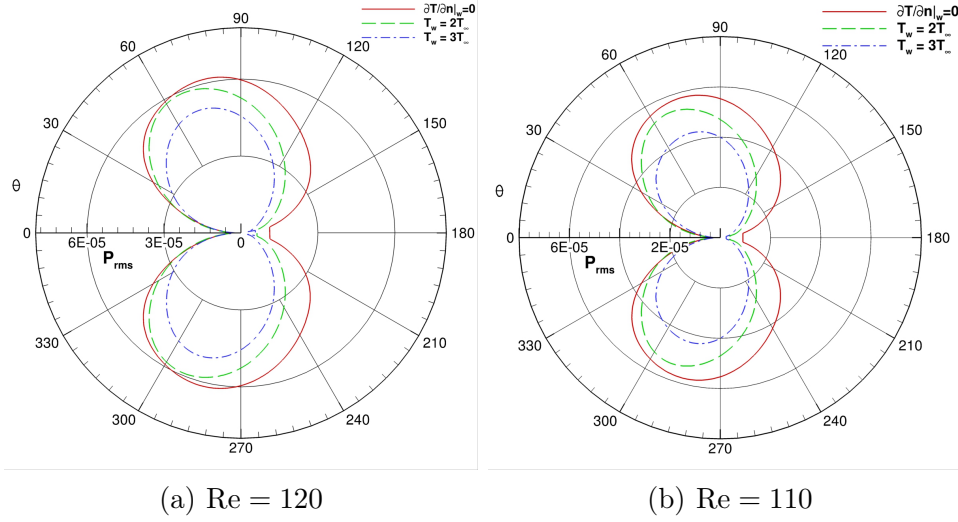


Figure 18. Wall temperature effect, square cylinder.  $p'_{rms}$ ,  $r/D = 40$ .

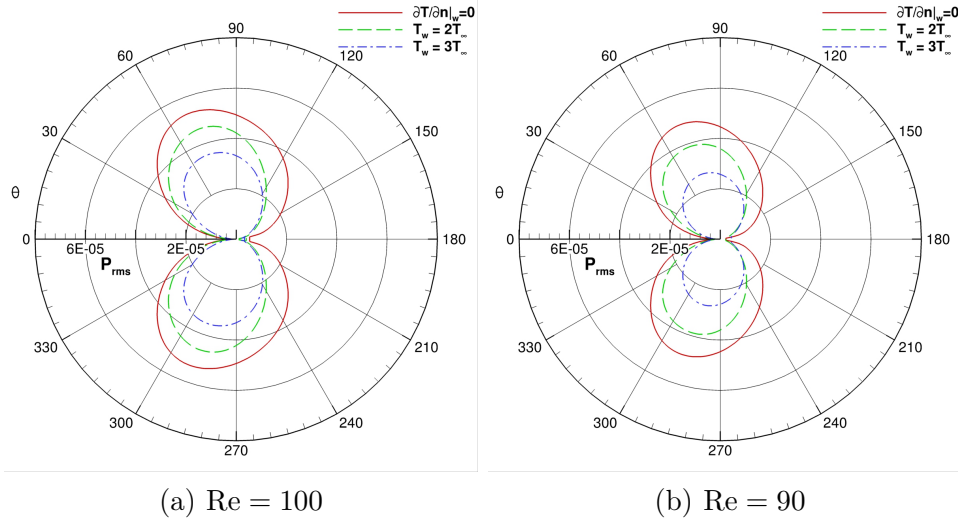


Figure 19. Wall temperature effect, square cylinder.  $p'_{rms}$ ,  $r/D = 40$ .

## 5 Conclusions

This paper addresses the development and application of an open-source solver for compressible mass, momentum and energy equations, named `caafFoam`, which is able to capture a wide range of flow phenomena. Particular attention was devoted to computing aeroacoustic sound. Our solver was developed within the FV OpenFOAM library and it adopts explicit low-storage Runge-Kutta schemes for time integration. KNP and Pirozzoli energy conserving schemes were used to handle Eulerian numerical fluxes, while standard central schemes were considered for diffusive terms. Only the Pirozzoli schemes proved capable of predicting acoustic waves on fully unstructured computational grids, while the two different approaches performed equally well on structured grids. An appropriate non-reflective boundary treatment

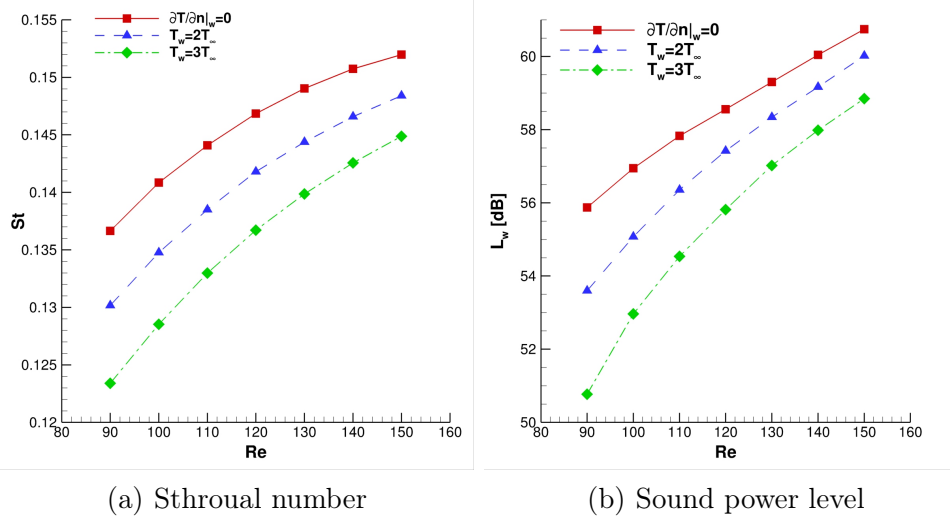


Figure 20. Wall temperature effect, square cylinder.

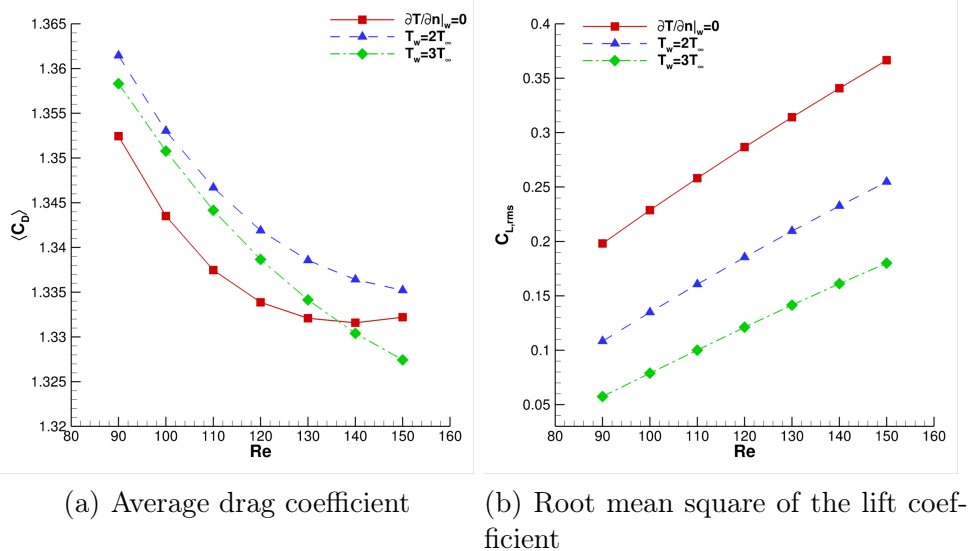


Figure 21. Wall temperature effect, circular cylinder. Force coefficients.

was achieved using an artificial sponge layer because it is simple to code, robust, and not stiff; and it proved flexible in handling complex geometries. The solver also showed a very good parallel performance on two completely different architectures, making it suitable for use in massively parallel aeroacoustic computations.

A broad range of far-field aeroacoustic sound configurations, emitted from bluff-bodies in a flow with uniform velocity inlet, was investigated for validation purposes. In all the benchmarks considered, `caafFoam` performed well in predicting the sound produced by the flow-body interaction. We found `rhoCentralFoam` unable to capture acoustic wave propagation phenomena correctly, even though we had introduced a proper non-reflective boundary treatment. On the other hand, the `caafFoam-m1` version can produce a direct

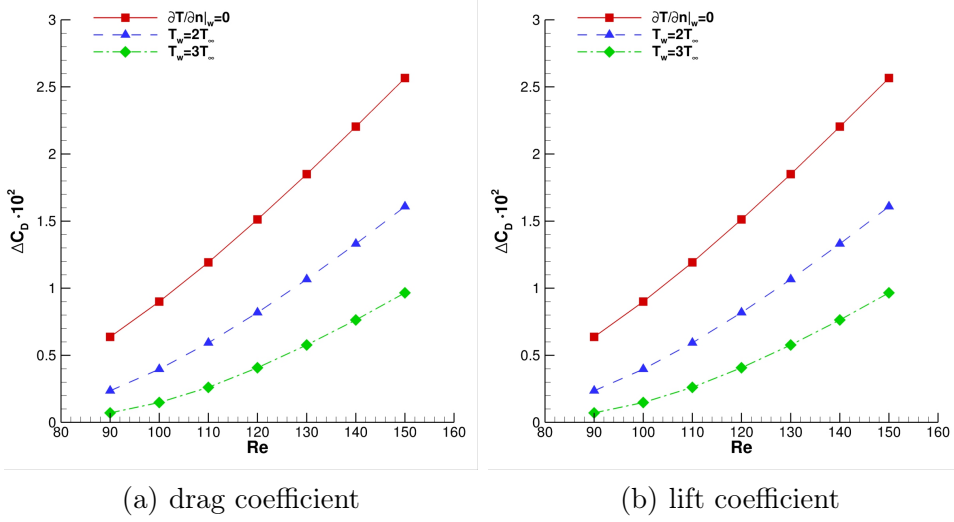


Figure 22. Wall temperature effect, circular cylinder. Force coefficients fluctuations.

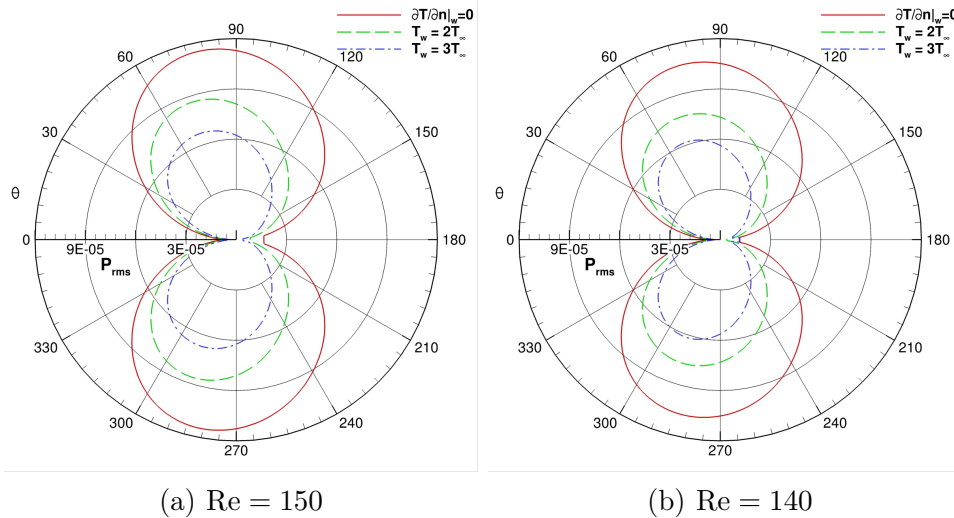


Figure 23. Wall temperature effect, circular cylinder.  $p'_{rms}$ ,  $r/D = 40$ .

solution of aeroacoustic fields. This goes to show that the inviscid numerical flux is not the key ingredient on structured grids; the solution algorithm is the primary issue to address.

Another novelty of this paper concerns our assessment of the impact of thermal boundary conditions at the wall on the sound produced by the interaction of a bluff body with a uniform laminar flow. Two different cases were considered, with square and circular cylinders. In both cases, we found that heating the wall reduces the vortex shedding developing in the wake region, as noted experimentally by Lecordier et al. [8]. This is of considerable interest in aeroacoustics because the pulsations of the lift and drag forces for these objects are directly related to the aerodynamically-produced sound. In fact, reducing them by heating the wall in turn reduces the production of acoustic perturbations. In other words, increasing the wall temperature reduces the sound

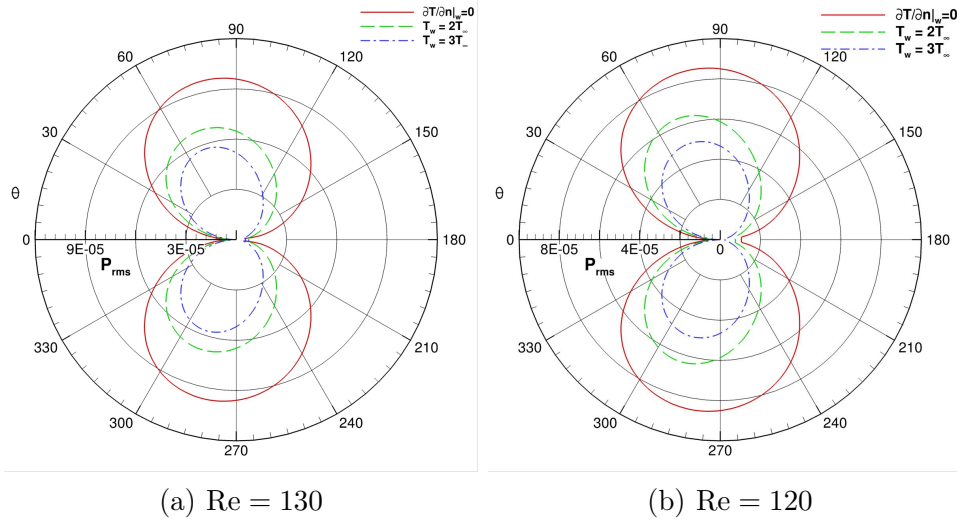


Figure 24. Wall temperature effect, circular cylinder.  $p'_{rms}$ ,  $r/D = 40$ .

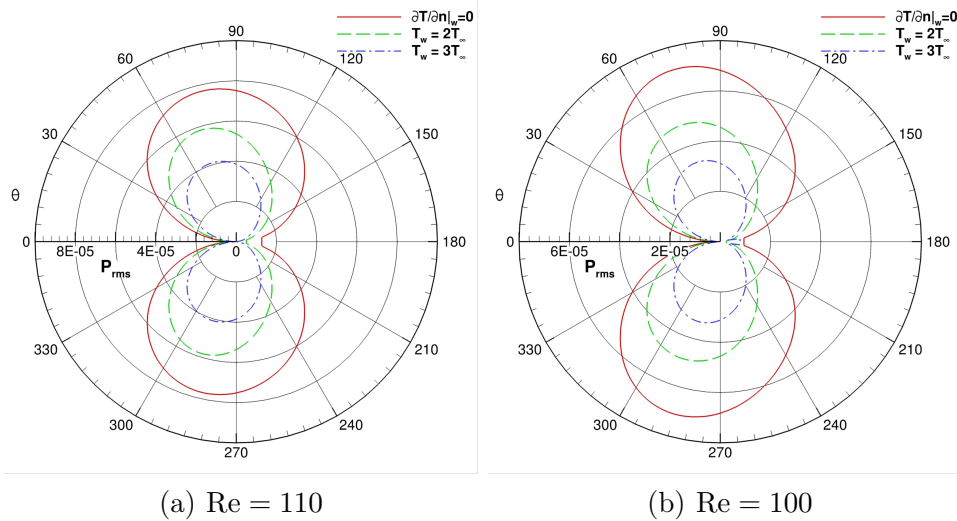


Figure 25. Wall temperature effect, circular cylinder.  $p'_{rms}$ ,  $r/D = 40$ .

power level. This finding has important practical implications since it can be considered as a method for actively controlling aeroacoustic sound.

## 6 Acknowledgements

We acknowledge the CINECA Award N. HP10CG4PUI YEAR 2018 under the ISCRA initiative, for the availability of high performance computing resources and support. We acknowledge the CINECA Award N. HP10CQ7QS7 YEAR 2019 under the ISCRA initiative, for the availability of high performance computing resources and support. We acknowledge the type-A preparatory PRACE project 2010PA4840 YEAR 2019 for the availability of high performance computing resources and support.

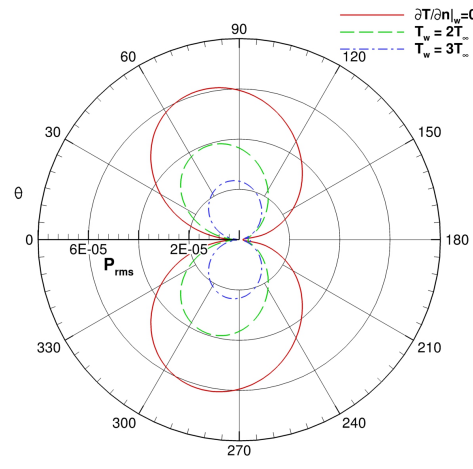
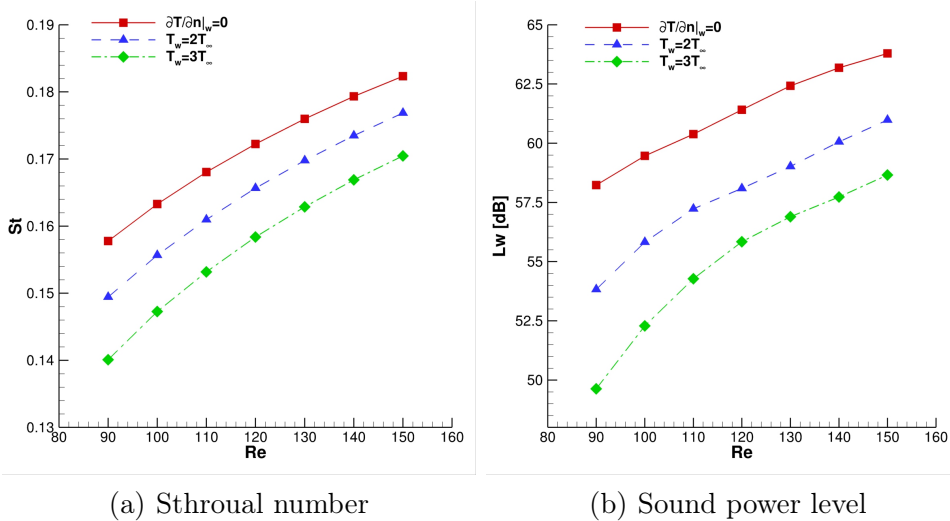


Figure 26. Wall temperature effect, circular cylinder.  $p'_{rms}$ ,  $r/D = 40$ .



(a) Sthroual number

(b) Sound power level

Figure 27. Wall temperature effect, circular cylinder.

## References

- [1] S. K. Lele and J.W. Joseph. A second golden age of aeroacoustics? *Philosophical Transactions of the Royal Society of London A: Mathematical, Physical and Engineering Sciences*, 372(2022), 2014.
- [2] T. Tim Colonius and S.K. Lele. Computational aeroacoustics: progress on nonlinear problems of sound generation. *Progress in Aerospace Sciences*, 40(6):345 – 416, 2004.
- [3] C.K.W. Tam. Computational aeroacoustics: An overview of computational challenges and applications. *International Journal of Computational Fluid Dynamics*, 18(6):547–567, 2004.
- [4] P.J. Morris, L.N. Long, T.E. Scheidegger, and S. Boluriaan. Simulations of supersonic jet noise. *International Journal of Aeroacoustics*, 1(1):17–41, 2002.

- [5] M. Lorteau, F. Clero, and F. Vuillot. Analysis of noise radiation mechanisms in hot subsonic jet from a validated les solution. *Physics of Fluids*, 27(17), 2015.
- [6] H.M. Frank and C.D. Munz. Direct aeroacoustic simulation of acoustic feedback phenomena on a side-view mirror. *Journal of Sound and Vibration*, 371:132 – 149, 2016.
- [7] B. Cockburn, G.E. Karniadakis, and C.W. Shu. *Discontinuous Galerkin Methods – Theory, Computations and Applications*. Springer–Verlag, Berlin, 2000.
- [8] J.C. Lecordier, L. Hamma, and P. Paranthoen. The control of vortex shedding behind heated circular cylinders at low reynolds numbers. *Experiments in Fluids*, 10(4):224–229, 1991.
- [9] J.-C. Lecordier, L.W.B. Browne, S. Le Masson, F. Dumouchel, and P. Paranthoen. Control of vortex shedding by thermal effect at low reynolds numbers. *Experimental Thermal and Fluid Science*, 21(4):227–237, 2000.
- [10] M. Israeli and S.A. Orszag. Approximation of radiation boundary conditions. *Journal of Computational Physics*, 41:115–135, 1981.
- [11] D.J. Bodony. Analysis of sponge zone for computational fluid mechanics. *Journal of Computational Physics*, 212:681–702, 2006.
- [12] T. Ikeda, T. Takashi Atobe, and S. Takagi. Direct simulations of trailing–edge noise generation from two-dimensional airfoils at low Reynolds numbers. *Journal of Sound and Vibration*, 331(3):556 – 574, 2012.
- [13] A. Mani. Analysis and optimization of numerical sponge layers as a nonreflective boundary treatment. *Journal of Computational Physics*, 231(2):704–716, 2012.
- [14] G. Kreiss, B. Krank, and G. Efraimsson. Analysis of stretched grids as buffer zones in simulations of wave propagation. *Applied Numerical Mathematics*, 107:1 – 17, 2016.
- [15] A. Kurganov, S. Noelle, and G. Petrova. Semidiscrete central–upwind schemes for hyperbolic conservation laws and Hamilton–Jacobi equations. *SIAM Journal on Scientific Computing*, 23:707–740, 2001.
- [16] C.J. Greenshields, H.G. Weller, L. Gasparini, and J.M. Reese. Implementation of semi-discrete, non-staggered central schemes in a colocated, polyhedral, finite volume framework, for high-speed viscous flows. *International Journal for Numerical Methods in Fluids*, 63(1):1–21, 2010.
- [17] S. Pirozzoli. Generalized conservative approximations of split convective derivative operators. *Journal of Computational Physics*, 229(19):7180 – 7190, 2010.
- [18] F. Ducros, V. Ferrand, F. Nicoud, C. Weber, D. Darracq, C. Gacherieu, and T. Poinsot. Large–Eddy Simulation of the Shock/Turbulence Interaction. *Journal of Computational Physics*, 152(2):517 – 549, 1999.
- [19] S. Pirozzoli. Numerical methods for high-speed flows. *Annual Review of Fluid Mechanics*, 43:163–194, 2011.
- [20] D. Modesti and S. Pirozzoli. A low–dissipative solver for turbulent com-

- pressible flows on unstructured meshes, with OpenFOAM implementation. *Computers & Fluids*, 152:14 – 23, 2017.
- [21] M. S. Liou. A sequel to AUSM, Part II: AUSM+-up for all speeds. *Journal of Computational Physics*, 214(1):137 – 170, 2006.
  - [22] J.H. Ferziger and M. Peric. *Computational Methods for Fluid Dynamics*. Springer, 1999.
  - [23] J.H Williamson. Low-storage Runge–Kutta schemes. *Journal of Computational Physics*, 35(1):48 – 56, 1980.
  - [24] C.A. Kennedy, M.H. Carpenter, and R.M. Lewis. Low-storage, explicit Runge–Kutta schemes for the compressible Navier–Stokes equations. *Applied Numerical Mathematics*, 35(3):177 – 219, 2000.
  - [25] M.H. Carpenter and C.A. Kennedy. Third order 2N–storage Runge–Kutta schemes with error control. Technical Memorandum 109111, NASA, 1994.
  - [26] H.G. Weller, G. Tabor, H. Jasak, and C. Fureby. A tensorial approach to computational continuum mechanics using object–oriented techniques. *Computational Physics*, 12(6):620–631, 1998.
  - [27] V. Vuorinen, J.-P. Keskinen, C. Duwig, and B.J. Boersma. On the implementation of low-dissipative Runge–Kutta projection methods for time dependent flows using OpenFOAM. *Computers & Fluids*, 93:153 – 163, 2014.
  - [28] OpenCFD Ltd. OpenFOAM programmer’s guide, 2016. [www.openfoam.com](http://www.openfoam.com).
  - [29] G. Axtmann and U. Rist. Scalability of OpenFOAM with Large Eddy Simulation and DNS on HPC Systems. In *High Performance Computing in Science and Engineering*, Germany, 2016.
  - [30] M. Culpo. Current Bottlenecks in the Scalability of OpenFOAM on Massively Parallel Clusters, 2011. PRACE white paper, available on [www.prace-ri.eu](http://www.prace-ri.eu).
  - [31] V. D’Alessandro, S. Montelpare, and R. Ricci. Detached–eddy simulations of the flow over a cylinder at  $Re = 3900$  using OpenFOAM. *Computers & Fluids*, 136:152–156, 2016.
  - [32] [www.prace-ri.eu](http://www.prace-ri.eu). Partnership for Advanced Computing in Europe.
  - [33] B. Muller. High order numerical simulation of aeolian tones. *Computers and Fluids*, 37:450–462, 2008.
  - [34] O. Inoue and N. Hatakeyama. Sound generation by a two-dimensional circular cylinder in a uniform flow. *Journal of Fluid Mechanics*, 471:285–314, 2002.
  - [35] M. Dumbsler. Arbitrary high order PNPM schemes on unstructured meshes for the compressible Navier–Stokes equations. *Computers & Fluids*, 39(1):60–76, 2010.
  - [36] N. Ganta, B. Mahato, and Y.G. Bhumkar. Analysis of sound generation by flow past a circular cylinder performing rotary oscillations using direct simulation approach. *Physics of Fluids*, 31(2), 2019.
  - [37] N. Ganta, B. Mahato, and Y.G. Bhumkar. Modulation of sound waves

- for flow past a rotary oscillating cylinder in a non-synchronous region. *Physics of Fluids*, 31(9), 2019.
- [38] Ruixian Ma, Zhansheng Liu, Guanghui Zhang, Con J. Doolan, and Danielle J. Moreau. Control of Aeolian tones from a circular cylinder using forced oscillation. *Aerospace Science and Technology*, 94:105370, 2019.
- [39] S. Kang. Characteristics of flow over two circular cylinders in tandem and side-by-side arrangement. *Physics of Fluids*, 15, 2003.
- [40] O. Inoue, W. Iwakami, and N. Hatakeyama. Aeolian tones radiated from flow past two square cylinders in a side-by-side arrangement. *Physics of Fluids*, 18, 2006.
- [41] W.K. Blake. *Mechanics of Flow induced Sound and Vibration*. Academic, New York, 1986.
- [42] O. Inoue, M. Mori, and N. Hatakeyama. Aeolian tones radiated from flow past two square cylinders in tandem. *Physics of Fluids*, 18(4), 2006.
- [43] W. Blake. *Mechanics of flow-induced sound and vibrations*. Elsevier, New York, 2017.
- [44] Kim, J., and Koratkar, N., and Rusak, Z. Small-Scale Airfoil Aerodynamic Efficiency Improvement by Surface Temperature and Heat Transfer. *AIAA Journal*, 41:2105–2112, 2012.
- [45] Bekka, N. and Sellam, M. and Chpoun, A. Numerical Study of Heat Transfer Around the Small Scale Airfoil Using Various Turbulence Models. *Numerical Heat Transfer, Part A: Applications*, 56:946–969, 2009.
- [46] Hinz, F.D., and Alighanbari, H., and Breitsamter, C. Influence of heat transfer on the aerodynamic performance of a plunging and pitching NACA0012 airfoil at low Reynolds numbers. *Journal of Fluids and Structures*, 37:88–99, 2013.
- [47] C.H.K. Williamson. Vortex dynamics in the cylinder wake. *Annual Review of Fluid Mechanics*, 28:477–539, 1996.